J. Fluid Mech. (1991), *vol.* 227, *pp.* 211–244
Printed in Great Britain

Particle dynamics and mixing in a viscously decaying shear layer

By E. MEIBURG[1]† AND P. K. NEWTON[2]

[1] Division of Applied Mathematics, Brown University, Providence, RI 02912, USA

[2] Department of Mathematics, University of Illinois, Urbana, IL 61801, USA

Received 30 December 1989 and in revised form 19 September 1990)

We study the mixing of fluid in a viscously decaying row of point vortices. To this end, we employ a simplified model based on Stuart's (1967) one-parameter family of solutions to the steady Euler equations. Our approach relates the free parameter to a vortex core size, which grows in time according to the exact solution of the Navier–Stokes equations for an isolated vortex. In this way, we approach an exact solution for small values of t/Re. We investigate how the growing core size leads to a shrinking of the cat's eye and hence to fluid leaking out of the trapped region into the free streams. In particular, we observe that particles initially located close to each other in neighbouring intervals along the streamwise direction escape from the cat's eye near opposite ends. The size of these intervals scales with the inverse square root of the Reynolds number. We furthermore examine the particle escape times and observe a self-similar blow-up for the particles near the border between two adjacent intervals. This can be explained on the basis of a simple stagnation-point flow. An investigation of interface generation shows that viscosity leads to an additional factor proportional to time in the growth rates. Numerical simulations confirm the above results and give a detailed picture of the underlying mixing processes.

1. Introduction

The mixing of two fluids is of considerable interest in a variety of natural and technical processes. The spreading of pollutants in the atmosphere, in rivers, oceans or groundwater reservoirs, for example, falls into the first category, whereas applications might concern the efficient mixing of two reacting species in a chemical reactor or a combustion chamber. Depending on the specific problem, either convective or diffusive effects can dominate, although often both of them are essential. In this paper, we attempt to study the fluid mixing that occurs in an unsteady non-periodic two-dimensional prototype flow involving viscous as well as inertial effects, namely in a viscously decaying row of point vortices. This idealized situation is relevant for temporally evolving mixing layers. Our interest focuses on the mixing of a passive scalar, i.e. we will study the dynamics of tracer particles that faithfully follow the fluid.

Recently, several researchers have addressed the problem of mixing of a passive scalar in incompressible flow from the dynamical systems point of view. Using the analytical tools provided by dynamical systems theory, one can show that many simple unsteady laminar flows are non-integrable, and hence can give rise to chaotic

† Present address: Department of Aerospace Engineering, University of Southern California, Los Angeles, CA 90089, USA.

particle trajectories, thus resulting in efficient mixing. This observation forms the basis of what has become known as chaotic advection (Aref 1984) or Lagrangian turbulence (Dombre *et al.* 1986). In order to exploit the powerful concepts related to dynamical systems theory, almost all the work performed so far concerns two-dimensional potential or Stokes flow with periodic perturbations or three-dimensional steady flows at finite Reynolds numbers. Thus, the unsteady velocity fields investigated in the past represent opposite ends of the Reynolds-number spectrum: momentum is transported exclusively by convection or diffusion, respectively.

The work by Aref & Balachandar (1986) on chaotic advection in Stokes flow clearly demonstrates that a smooth Eulerian velocity field can lead to chaotic particle paths. In other words, Lagrangian turbulence can be expected to occur even at vanishing Reynolds numbers, whereas Eulerian turbulence is usually observed only for Reynolds numbers exceeding a certain threshold value. Jones & Aref (1988) furthermore show that circulation is not a necessary ingredient for obtaining chaotic advection; unsteady irrotational velocity fields as well have the ability to efficiently stir passive scalars. Aref & Jones (1989) investigate the interplay of reversible Stokes flow and particle diffusion, modelled in a random walk fashion, to maximize the rate at which diffusing particles can separate. Khakhar, Rising & Ottino (1986) study some of the above as well as other flows in more detail, employing dynamical systems theory. The work of Rom-Kedar, Leonard & Wiggins (1990) concerns the case of a translating point-vortex pair perturbed by a small-amplitude time-periodic flow. By applying Melnikov's analysis, they demonstrate the existence of Smale horseshoes leading to chaotic particle dynamics and hence to efficient mixing of the fluid near the unperturbed separatrices. Flows involving finite-Rayleigh-number effects in convection have been studied by Arter (1983) and Solomon & Gollub (1988). Finite-Reynolds-number effects are also included in the paper by Jones, Thomas & Aref (1989) on steady flow through a twisted pipe. Finally, Broomhead & Ryrie (1988) study particle transport between Taylor vortices near the onset of instability as a function of perturbation amplitude. While most of the above contributions represent combinations of analytical and numerical work, Ottino & co-workers have also performed a series of experimental studies concerning chaotic advection in smooth flows. References, as well as many instructive pictures of flow visualization experiments, can be found in the recent book by Ottino (1989), which contains an excellent collection of material concerned with the kinematic aspects of mixing. Experimental work has also been reported by Chaiken *et al.* (1986).

Two-dimensional unsteady finite-Reynolds-number flows such as the viscously decaying row of point vortices to be considered in this paper, on the other hand, are often non-periodic, and hence the related mixing processes are not as amenable to an analysis based on dynamical systems theory. In particular, powerful concepts such as Poincaré sections are of limited help. Enhanced mixing occurs even though the underlying flow field does not give rise to chaotic advection. Hence, in the present paper, we have to resort to other analytical and numerical means to study quantities of interest such as, for example, interfacial stretching rates. Some guidance can be found in earlier work studying particle transport in an inviscid, i.e. non-decaying row of point vortices corresponding to the well-known streamline pattern of the Kelvin cat's eyes. In particular, Jimenez (1980) modelled the entrainment and mixing between two streams initially separated by a straight interface on the basis of an infinite row of point vortices placed along the interface. In this time-independent velocity field, he observes the progressive stretching and folding of the interface into

the form of spirals around the point vortices. In this way, the interfacial arclength between the two fluids grows continuously within the cat's eye. No fluid is exchanged between the interior and the exterior of the cat's eye, as the streamline pattern does not change in time. However, Jimenez finds that, if in addition he allows for pairing, this simple model reproduces the visual growth rate quite well.

Roberts (1985) modifies the above analysis and studies the case in which the row of point vortices is displaced into the faster stream a small distance away from the interface. This approach can be rationalized by remembering that the dominant sign of vorticity comes from the boundary layer of the faster stream. It has the further advantage of simplifying the computational interface tracking, as it avoids the problem of velocity singularities. Roberts also considers various degrees of concentration of the vorticity by employing Stuart's (1967) one-parameter family of solutions to the Euler equations. He presents numerically integrated interfacial shapes for various parameter combinations and finds good qualitative agreement with experimental observations.

In the present paper, we will add the effect of viscous decay to the problem, and it will become evident how this aspect fundamentally changes the nature of the flow, especially as far as the mixing between different fluid regions is concerned. Our starting point is the well-known fact that the equations of motion for passively advected particles in an unsteady two-dimensional incompressible flow are given by

$$\frac{\mathrm{d}x}{\mathrm{d}t} = \frac{\partial \psi}{\partial y}; \quad \frac{\mathrm{d}y}{\mathrm{d}t} = -\frac{\partial \psi}{\mathrm{d}x}. \tag{1}$$

Here $\psi(x, y, t)$ has the interpretation of a time-dependent stream function. Since (1) also takes the form of Hamilton's canonical equations of motion, $\psi(x, y, t)$ can be interpreted as a time-dependent one-degree-of-freedom Hamiltonian for the flow (see Aref 1984). Hence, a given stream function completely determines the subsequent particle paths whose coordinates are $(x(t), y(t))$. Our goal is to introduce a model which captures the effects of viscous decay in a shear layer since we do not have analytical solutions to the full Navier–Stokes equations available. We then use this model to study the dynamics and mixing of particles as they move through this shear layer. The same problem could, in principle, be studied by direct numerical simulation of the Navier–Stokes equations; however, an advantage to our approach is its simplicity which allows us to make analytical progress.

Our model is based on Stuart's one-parameter family of solutions to the two-dimensional Euler equations (Stuart 1967; Pierrehumbert & Widnall 1981)

$$\tilde{\psi}(\tilde{x}, \tilde{y}) = \frac{l \Delta U}{4\pi} \ln \left[\cosh\left(\frac{2\pi \tilde{y}}{l}\right) - \rho \cos\left(\frac{2\pi \tilde{x}}{l}\right) \right], \tag{2}$$

where l is the distance between two vortices and ΔU is the velocity difference between the two streams forming the shear layer. We normalize the solution by taking l and $\Delta U/4\pi$ as the characteristic scales for length and velocity, respectively. The dimensionless stream function $\psi(x, y)$ then becomes

$$\psi(x, y) = \ln \left[\cosh(2\pi y) - \rho \cos(2\pi x) \right]. \tag{3}$$

The parameter ρ indicates the concentration of vorticity: $\rho = 1$ corresponds to a periodic row of point vortices, $\rho = 0$ corresponds to parallel shear flow. The streamlines for this solution trace out the well-known cat's eye shown in figure 2(*a*). In the model to be presented in this paper, we will relate the free parameter ρ, which

determines the shape of the cat's eye, to the vortex core size. Subsequently, we will simulate the effect of viscosity by letting this core size grow in time in analogy to the Oseen vortex, which represents a self-similar solution to the Navier–Stokes equations describing the viscous growth of an isolated vortex core (e.g. Panton 1979). As a result of the core growth, the cat's eyes, i.e. the separatrices, shrink in time which leads to new and interesting phenomena. While in the inviscid case, fluid initially within the cat's eye does not mix with the outside fluid, viscosity causes the trapped fluid to leak out of the cat's eye. Furthermore, different fluid regions initially trapped mix much more efficiently under the effect of small viscosity. Owing to the effect of viscosity, the flow becomes explicitly time-dependent; thus a particle which is initially trapped within the cat's eye will escape through a separatrix at some finite time. This leads to an infinite number of alternating layers within the cat's eye which become infinitesimally thin near the vortex centre. These layers characterize initial data according to whether a particle will escape above the mixing layer and continue moving right, or below the mixing layer and continue moving left. The process of crossing the separatrix in the flow is the essential mechanism which leads to sensitive behaviour and enhanced mixing. This theory has been developed and exploited in other contexts, see for example Timofeev (1978), Tennyson, Cary & Escande (1986), as well as Bourland & Haberman (1990). In the present paper, we focus on quantities that characterize the mixing of fluids, such as local and global interface stretching rates, fluxes across separatrices etc.

The paper is structured in the following way. Section 2 contains a discussion of the model we use to simulate the effects of viscosity on the shear layer. The rationale for the model is described, as are its limitations. In §3 we describe a convenient mathematical tool we use in following the background flow and evolution of the phase plane. The background flow for the decaying shear layer is described and the reasons for the presence of the alternating layers inside a shrinking cat's eye are explained. Section 4 describes a scaling theory which shows how the alternating layers scale with the Reynolds number. We compare our theory with numerical simulations and find close agreement. In addition, we compute the flux of the fluid across the separatrix. In §5 we describe results which predict the escape times for particles starting inside the mixing layer to exit from the cat's eye. Section 6 contains a discussion of particle and fluid mixing and the role which viscosity plays in this problem. We also describe the phenomenon of interface stretching. Finally, §7 contains a discussion of the various shortcomings of the model as well as current and future directions.

2. Viscous model

A well-known self-similar solution to the radially symmetric Navier–Stokes equations, known as the Oseen vortex, has a velocity profile given by

$$v_\theta(r,t) = \frac{\Gamma}{2\pi r}\left(1-\exp\left(-\frac{r^2}{4\nu t}\right)\right). \tag{4}$$

Here v_θ is the solution to the θ-direction momentum equation, Γ is the circulation, and ν is the viscosity. If we introduce the Reynolds number $Re = \Gamma/\nu$ and normalize so that $\Gamma = 1$, we can interpret the above velocity field as that of a viscously diffusing point vortex, whose core size σ grows like $\sigma = (4\nu t)^{\frac{1}{2}} = (4t/Re)^{\frac{1}{2}}$ (Paton 1979). The first goal is to incorporate this behaviour into our model. It is straightforward to see that

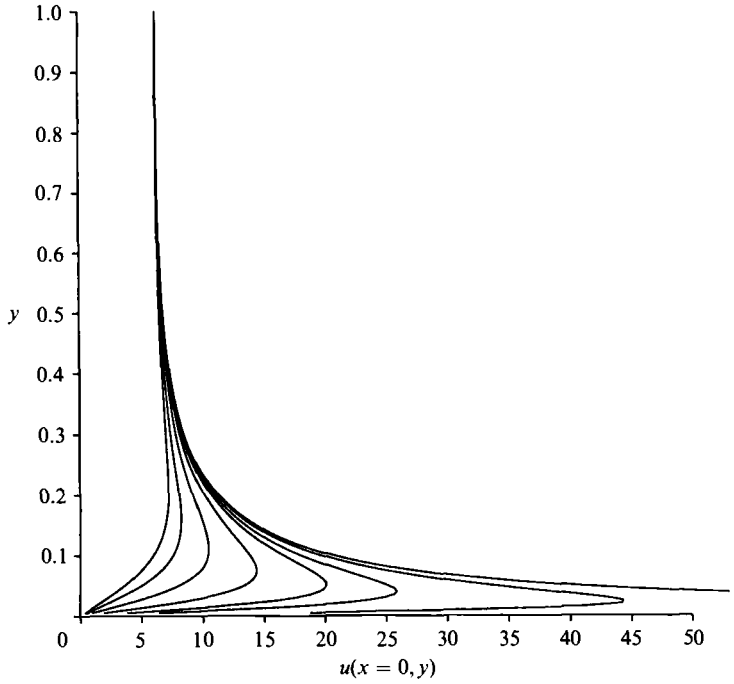

FIGURE 1. The u-velocity profile for the cat's eye at $x = 0$. The profiles correspond (from right to left) to values for ρ of 1, 0.99, 0.97, 0.95, 0.9, 0.8, 0.65, and 0.5. Notice how the velocity profile changes from that corresponding to a row of point vortices to that of a plane shear layer as the value of ρ decreases.

the cat's eye of the Stuart vortex (3) is widest at the origin $x = 0$. The y-coordinate of the separating streamline along this line is then given by

$$y_w = \frac{1}{2\pi}\cosh^{-1}(1+2\rho). \tag{5}$$

We would like to relate ρ to a core size which we then let grow in time. To do this, it is useful to look at the velocity profile of the Stuart vortex shown in figure 1. From this, it seems natural to define the core size, σ, as the vertical distance from the origin to $y(u = u_{\max})$, where $u_{\max}$ is the maximal velocity in the x-direction. From (3) we see that

$$\psi(x = 0, y) = \ln(\cosh(2\pi y) - \rho). \tag{6}$$

This gives a formula for the x-component of velocity from (1):

$$u(x = 0, y) = \frac{\partial \psi}{\partial y}(x = 0, y) = \frac{2\pi \sinh(2\pi y)}{\cosh(2\pi y) - \rho}. \tag{7}$$

From this we compute $\partial u/\partial y\ (x = 0, y)$:

$$\frac{\partial u}{\partial y}(x = 0, y) = \frac{4\pi^2(1 - \rho\cosh(2\pi y))}{(\cosh(2\pi y) - \rho)^2}. \tag{8}$$

Setting the numerator of (8) to zero and solving for y gives $y(u = u_{\max})$,

$$y(u = u_{\max}) \equiv \sigma = \frac{1}{2\pi}\cosh^{-1}\left(\frac{1}{\rho}\right). \tag{9}$$

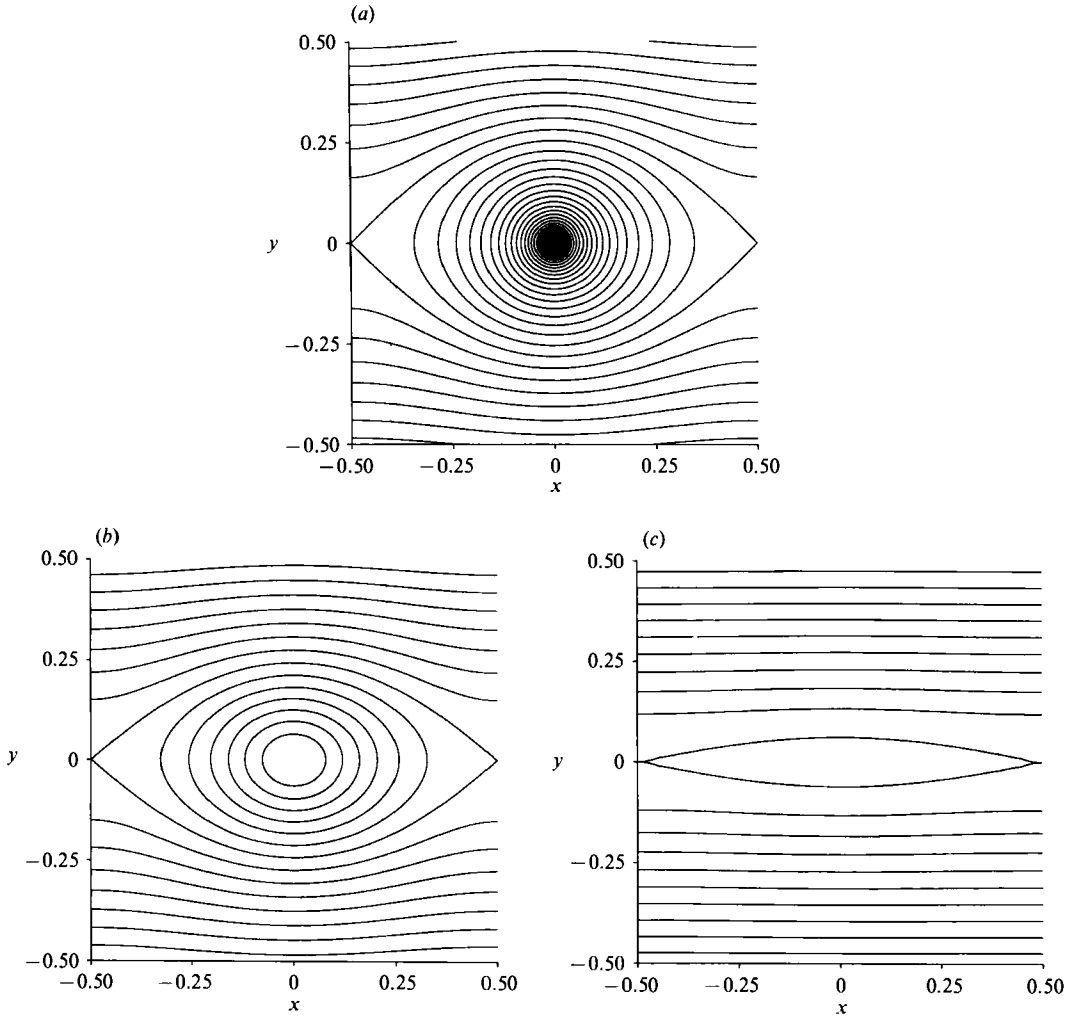

FIGURE 2. Our model for the viscous growth of the vortex cores leads to a variation of the streamline pattern with time. Shown are snapshots of instantaneous streamline patterns for values of t/Re of (*a*) 0, (*b*) 0.005 and (*c*) 0.1. Notice how the cat's eye shrinks in time, thus trapping less and less fluid.

We then let $\sigma = (4t/Re)^{\frac{1}{2}}$ and invert (9) to obtain

$$\rho(t) = \frac{1}{\cosh\left[4\pi\left(\frac{t}{Re}\right)^{\frac{1}{2}}\right]}. \tag{10}$$

Thus $\rho(0) = 1$ corresponds to the periodic row of point vortices and $\rho(\infty) = 0$ corresponds to parallel shear flow. The width of the cat's eye, y_w, given by (5) then goes from a value of $y_w(t = 0) = (1/2\pi)\cosh^{-1}(3)$ initially to $y_w(t \to \infty) = 0$.

Thus, the time-dependent stream function for our model is given by the Stuart vortex (3), with the free parameter ρ evolving in time according to (10). Several snapshots of the instantaneous stream function are shown in figure 2. Here we show only one window ($-0.5 \leqslant x \leqslant 0.5$) of the flow field at various times. The flow field for

other windows is a periodic extension of that shown. Thus, our model takes into account the viscous diffusion of each point vortex as if it were isolated from the rest of the field. It does not, for example, take into account the effects of neighbouring vortices on the core growth and therefore does not include the effects of core deformation and filamentation seen in other works. For this reason, we expect our results to be applicable only for small values of the scaled variable t/Re. See Appendix A for a brief discussion of the error introduced by our model.

3. Phase plane dynamics

We next study in more detail the particle motion governed by (1). The equations of motion (1), (3), (10) give

$$\frac{\mathrm{d}x}{\mathrm{d}t} = \frac{2\pi \sinh(2\pi y)}{\cosh(2\pi y) - \rho(t)\cos(2\pi x)}, \tag{11}$$

$$\frac{\mathrm{d}y}{\mathrm{d}t} = \frac{-2\pi\rho(t)\sin(2\pi x)}{\cosh(2\pi y) - \rho(t)\cos(2\pi x)}. \tag{12}$$

The fixed points of (11), (12) are given by $y = 0$; $x_n = \pm\frac{1}{2}n$, where n is any positive integer. The nature of the fixed points is determined by the eigenvalues of the linearized flow, which yield

$$\lambda_n(t) = \frac{\pm(2\pi)^2}{(1-(-1)^n\rho)}((-1)^{n+1}\rho)^{\frac{1}{2}}. \tag{13}$$

Thus, for n even, the eigenvalues are purely imaginary, hence the fixed points are elliptic centres. These correspond to the vortex centres. For n odd, the eigenvalues are purely real and correspond to hyperbolic saddles. The evolution of the eigenvalues in the complex plane as time evolves are shown in figure 3. As the vortex core grows, the eigenvalues corresponding to the hyperbolic saddle move toward the origin. For this configuration the eigenvalues collide only in the limit $t \to \infty$. This signifies the disappearance of the cat's eye. For other configurations, collision of the eigenvalues can occur after a finite time, which has interesting consequences. This will be discussed in a separate publication.

In the absence of viscosity, the cat's eyes do not shrink and hence a particle initially trapped will remain trapped forever, undergoing periodic motion. Closed-form solutions can be derived for this case (Roberts 1985). The period of oscillation depends on the initial particle location and ranges from zero at the vortex centre to infinity at the separatrix. As a result of the viscous vortex core growth, a particle initially trapped within a cat's eye oscillating around the vortex centre will eventually escape through the separatrix. If the particle escapes above the x-axis ($y > 0$) it will continue travelling to the right above the mixing layer along the instantaneous streamlines shown in figure 2. If the particle escapes below the x-axis ($y < 0$) it will continue travelling to the left below the mixing layer. As a result, these two particles which both started within the cat's eye will separate, their distance going to infinity as time evolves. Figure 4 shows a schematic diagram of this process. There are infinitely many alternating intervals, l_n, along the x-axis inside the cat's eye, becoming increasingly thin as they approach the vortex centre. These layers characterize the initial particle positions according to whether a particle will escape

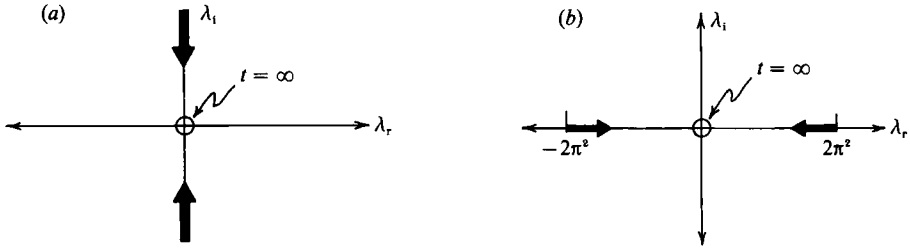

FIGURE 3. Evolution of eigenvalues: (*a*) n even, (*b*) n odd.

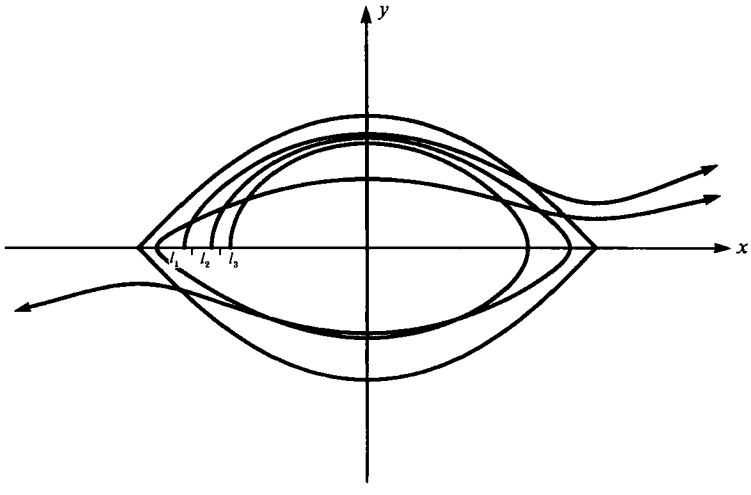

FIGURE 4. Schematic diagram of particles escaping from the cat's eye as a result of the shrinking of the trapped region due to viscosity. Actual particle paths are shown.

above the mixing layer (l_n, n odd) or below the mixing layer (l_n, n even). For example, a particle starting in the interval l_1 along the x-axis will escape through the top of the separatrix on its first half-cycle around the vortex centre. A particle starting in the interval l_2 will escape through the bottom of the separatrix on the second half-cycle. Since the particles travel faster the closer they are to the vortex centre, one can find a particle which loops around the centre an arbitrarily large number of times before it escapes by choosing its initial position to be arbitrarily close to the centre. This then implies that there must be an infinite number of these alternating layers getting increasingly thin but such that:

$$\sum_{n=1}^{\infty} l_n = \tfrac{1}{2}. \tag{14}$$

An important consequence of these layers is that one can find (near the vortex centre) an arbitrarily large number of particles which start infinitesimally close to each other but which ultimately separate in alternating directions, one above the mixing layer, the other below, the next above, etc. This enhances the mixing process and is a purely viscous effect.

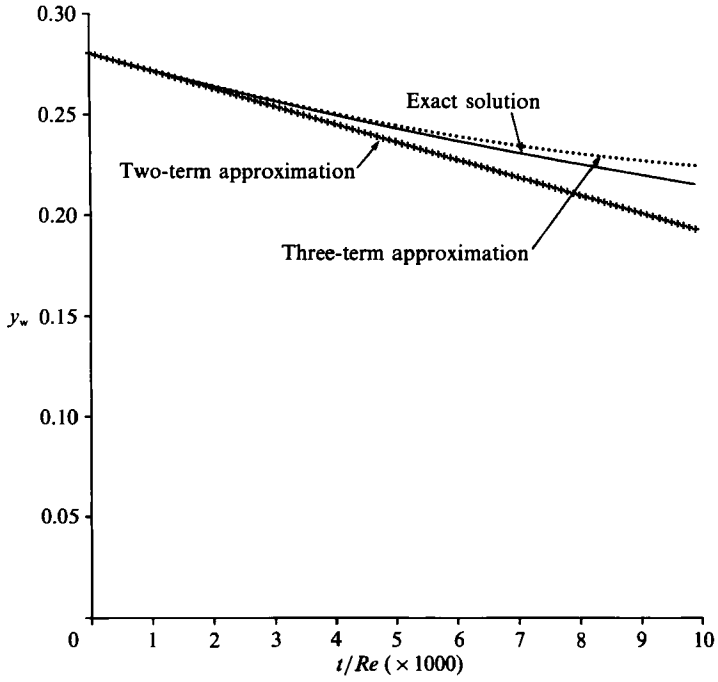

FIGURE 5. A comparison between the exact solution for $y_w(t/Re)$ according to our model and two- and three-term short-time expansions corresponding to (16).

4. Scaling results for the interval sizes

4.1. *Results for* l_1

To investigate how the interval lengths l_n depend on the parameter characterizing the flow, i.e. on the Reynolds number, we will employ series expansions valid for short times. This approach is consistent with the viscous model introduced in §2, which represents a close approximation to the real flow for small values of t/Re. We will justify this approach below by comparing our scaling results with a numerical simulation of the problem. As shown above, the half-width of the cat's eye varies with time as

$$y_w = \frac{1}{2\pi}\cosh^{-1}\left[1+\frac{2}{\cosh\left[2\pi\left(\frac{4t}{Re}\right)^{\frac{1}{2}}\right]}\right]. \tag{15}$$

By expanding in powers of (t/Re) we obtain the short-time expansion (for details, see Appendix B)

$$y_w = \frac{1}{2\pi}\cosh^{-1}(3)-\frac{\sqrt{8\pi}}{Re}t+\frac{22\sqrt{2\pi^3}}{3Re^2}t^2+O\left(\frac{t^3}{Re^3}\right) \tag{16}$$

for the half-width of the cat's eye. We find that the initial rate at which the width of the cat's eye decreases – as expressed by the $O(t/Re)$ term – is inversely proportional to the Reynolds number. Figure 5 compares the series expansion with the exact result (15). If we can now specify the time it takes for the cat's eye to shed the particles initially distributed along the interval l_1, we can compute the amount

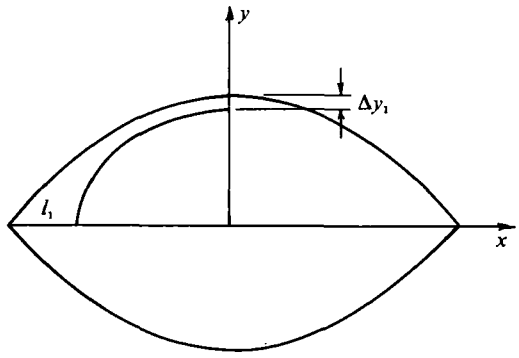

FIGURE 6. The particles crossing the y-axis in the interval Δy_1 originate from the x-axis interval Δx_1, i.e. l_1.

by which the width of the cat's eye decreases during that time, which in turn would allow us to obtain l_1. A slight complication arises through the fact that the particle marking the border between l_1 and l_2 stays within the cat's eye for an infinitely long time. Furthermore, neighbouring particles will stay within the cat's eye for finite but arbitrarily long times. This issue will be discussed in detail in §5. Consequently, we instead aim at obtaining an approximate value t_c for the time at which the shedding of l_1 is largely completed and the shedding of l_2 becomes the more dominating effect. For this purpose, we define as the characteristic velocity u_c the u-velocity at $x = 0$, $y = y_w$ at time $t = 0$, and as the characteristic length l_c we take half the perimeter of the cat's eye at $t = 0$. These quantities will then allow us to compute the characteristic time t_c as $t_c = l_c/u_c$. From the general form of the velocity (7), and with y_w given by (5), we obtain

$$u_c(\rho) = 4\pi\left(\frac{\rho}{1+\rho}\right)^{\frac{1}{2}}. \tag{17}$$

With (10) this yields the maximum velocity at the dividing streamline

$$u_c\left(\frac{t}{Re}\right) = 2\sqrt{2\pi} - \frac{4\sqrt{2\pi^3 t}}{Re} \tag{18}$$

so that the desired characteristic velocity becomes

$$u_c(t=0) = 2\sqrt{2\pi}. \tag{19}$$

The perimeter length, S, of the cat's eye can be computed from the equation governing the shape of the separatrix

$$\cosh(2\pi y) - \rho\cos(2\pi x) = 1+\rho. \tag{20}$$

With

$$S = \int_{-\frac{1}{2}}^{\frac{1}{2}} \left(1+\left(\frac{\mathrm{d}y}{\mathrm{d}x}\right)^2\right)^{\frac{1}{2}} \mathrm{d}x \tag{21}$$

we obtain

$$S = 2\int_0^{\frac{1}{2}} \left(1+\frac{\rho^2\sin^2(2\pi x)}{2\rho(1+\rho)(1+\cos(2\pi x))+\rho^2\sin^2(2\pi x)}\right)^{\frac{1}{2}} \mathrm{d}x. \tag{22}$$

However, we were unable to integrate this expression analytically. As our expression for the characteristic velocity was only an approximate one, an approximate value

for the perimeter length as well will be sufficient for the present purposes. Recognizing that the shape of the cat's eye is not too different from that of an ellipse with half-axes $\frac{1}{2}$ and y_w, we can estimate its half-length as

$$L = \tfrac{1}{2}\pi(\tfrac{1}{2}+y_w) \tag{23}$$

which yields

$$L(\rho) = \tfrac{1}{4}\pi+\tfrac{1}{4}\cosh^{-1}(1+2\rho). \tag{24}$$

By again assuming ρ to depend on time according to our viscous model, and by expanding in powers of t we obtain

$$L\left(\frac{t}{Re}\right) \equiv l_c = \tfrac{1}{4}\pi+\tfrac{1}{4}\cosh^{-1}(3)-\frac{\sqrt{2}\pi^2}{Re}t+O\left(\frac{t^2}{Re^2}\right). \tag{25}$$

This results in a leading-order estimate of the characteristic time t_c:

$$t_c = \frac{\frac{1}{4}\pi+\frac{1}{4}\cosh^{-1}(3)}{2\sqrt{2}\pi} = \frac{1}{8\sqrt{2}}+\frac{1}{8\sqrt{2}\pi}\cosh^{-1}(3). \tag{26}$$

We can now proceed to calculate the amount Δy_1 by which the half-width of the cat's eye decreases while the particles in l_1 are being shed from its interior as

$$\Delta y_1 \approx -\frac{\mathrm{d}y_w}{\mathrm{d}t}(t=0)\,t_c. \tag{27}$$

This results in

$$\Delta y_1 = \frac{1}{Re}(\tfrac{1}{4}\pi+\tfrac{1}{4}\cosh^{-1}(3)). \tag{28}$$

It is left now to translate Δy_1 into l_1 (figure 6). In a way that is consistent with the above approximations, we can establish this relationship for the time-independent flow field corresponding to $t = 0$. Owing to the acceleration of the fluid particles as they leave the vicinity of the stagnation point, the distance between the separatrix (20) and a nearby streamline ψ_ϵ,

$$\psi_\epsilon = \ln(\cosh(2\pi y)-\rho\cos(2\pi x)) = \ln(1+\rho-\epsilon), \tag{29}$$

varies strongly between the stagnation-point region and the widest part of the cat's eye. At $x = 0$, the y-coordinate of ψ_ϵ can be approximated as

$$\begin{aligned} y &= \frac{1}{2\pi}\cosh^{-1}(3-\epsilon) \\ &= \frac{1}{2\pi}\ln(3-\epsilon+(8-6\epsilon)^{\frac{1}{2}}) \\ &\approx \frac{1}{2\pi}\ln\left(3+\sqrt{8}-\epsilon\left(1+\frac{3}{\sqrt{8}}\right)\right) \end{aligned} \tag{30}$$

so that we obtain

$$\begin{aligned} y_w-y &= -\frac{1}{2\pi}\ln\left(1-\frac{\epsilon}{\sqrt{8}}\right) \\ &\approx \frac{\epsilon}{4\sqrt{2}\pi}. \end{aligned} \tag{31}$$

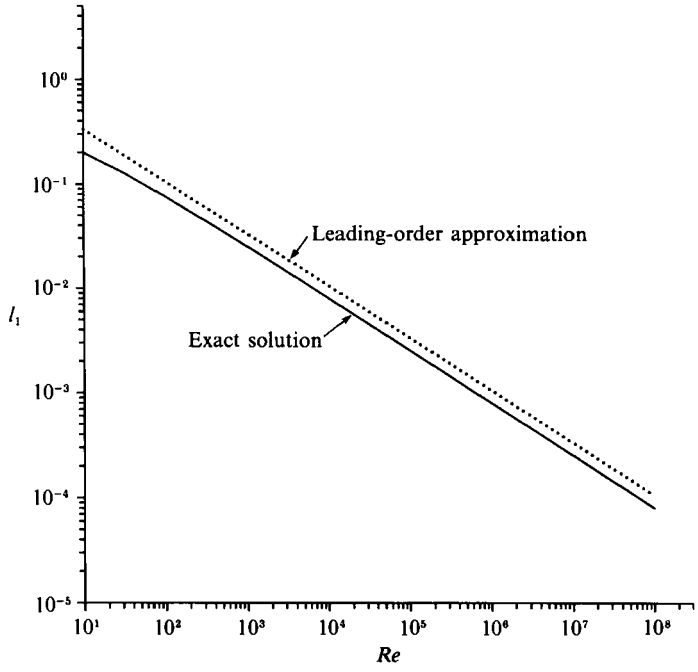

FIGURE 7. A comparison between the scaling result (34) and 'exact' numerical solutions for the interval size l_1 as a function of the Reynolds number. The numerical results confirm that l_1 scales with the inverse square root of Re.

Near the left stagnation point, on the other hand, ψ_ϵ is given by

$$\psi_\epsilon = \ln(1-\cos(2\pi x)) = \ln(2-\epsilon) \tag{32}$$

which can be expanded to obtain an approximation for the point at which ψ_ϵ crosses the x-axis

$$x = -\tfrac{1}{2} + \frac{1}{\sqrt{2\pi}}\epsilon^{\frac{1}{2}}. \tag{33}$$

Hence we recognize that the particles crossing the interval $\Delta y_1 \propto \epsilon$ emerge from a region $\Delta x_1 \propto \epsilon^{\frac{1}{2}}$ near the left stagnation point. Since we had found $\Delta y_1 \propto Re^{-1}$ we can conclude $\Delta x_1 \propto Re^{-\frac{1}{2}}$, i.e. that the interval l_1 scales with the inverse of the square root of the Reynolds number. With the above estimates for the characteristic time we obtain the quantitative relationship

$$\begin{aligned} l_1 &\approx \frac{1}{2^{\frac{1}{4}}(\pi Re)^{\frac{1}{2}}}(\pi + \cosh^{-1}(3))^{\frac{1}{2}} \\ &\approx Re^{-\frac{1}{2}}. \end{aligned} \tag{34}$$

It is straightforward to derive 'exact' numerical results by performing a time-dependent simulation and iterating for the initial particle position that results in infinite escape times from the interior of the cat's eye. Figure 7 compares the numerically obtained data for $l_1(Re)$ with relationship (34). It is obvious that for sufficiently large Re the functional dependence in the form of $Re^{-\frac{1}{2}}$ is satisfied very

well. The constant factor between the two curves is a result of the approximation entering the estimated characteristic time. Only for $Re < 100$ do we see a deviation from $Re^{-\frac{1}{2}}$. This is a consequence of the rapid growth of the vortex core at these low values of Re, which requires us to consider higher-order terms in the expansions for y_w and t_c as well.

4.2. *Results for* l_n

As a next step, we will derive scaling results for l_n, i.e. the lengths of x-axis intervals whose particles leave the cat's eye during successive half cycles. This is straightforward if we continue to limit ourselves to small values of t/Re. Then the leading-order approximation for the rate at which the width of the cat's eye decreases and for the characteristic time are still valid. We obtain

$$\Delta y_i = \Delta y_1, \quad i = 2, 3, \ldots, \tag{35}$$

i.e. each time the particles corresponding to one interval l_i escape, the cat's eye shrinks by the same amount. From the above results (31) and (33) for l_1 it follows with (35) that

$$\sum_{i=1}^{n} l_i = \frac{8^{\frac{1}{4}}}{(\pi)^{\frac{1}{2}}} \left(\sum_{i=1}^{n} \Delta y_i \right)^{\frac{1}{2}} \tag{36}$$

which yields

$$\begin{aligned} l_n &= \frac{8^{\frac{1}{4}}}{(\pi)^{\frac{1}{2}}} \left(\left(\sum_{i=1}^{n} \Delta y_i \right)^{\frac{1}{2}} - \left(\sum_{i=1}^{n-1} \Delta y_i \right)^{\frac{1}{2}} \right) \\ &= \frac{8^{\frac{1}{4}}}{\pi^{\frac{1}{2}}} (\Delta y_1)^{\frac{1}{2}} (n^{\frac{1}{2}} - (n-1)^{\frac{1}{2}}) \\ &= \frac{8^{\frac{1}{4}}}{\pi^{\frac{1}{2}}} Re^{-\frac{1}{2}} (\tfrac{1}{4}\pi + \tfrac{1}{4} \cosh^{-1}(3))^{\frac{1}{2}} (n^{\frac{1}{2}} - (n-1)^{\frac{1}{2}}). \end{aligned} \tag{37}$$

For $n \gg 1$, it is furthermore straightforward to show that

$$n^{\frac{1}{2}} - (n-1)^{\frac{1}{2}} \approx \frac{1}{2n^{\frac{1}{2}}}. \tag{38}$$

Keeping in mind that the constant factor is a result of the approximations leading to estimates for t_c we compare the scaling result

$$l_n \propto Re^{-\frac{1}{2}} (n^{\frac{1}{2}} - (n-1)^{\frac{1}{2}}) \tag{39}$$

and the numerically obtained results in figure 8 for $Re = 1000$. Here the value of the proportionality factor for the sake of comparison has been chosen so that the two sets of data agree for $n = 1$. We find reasonable agreement and thus confirm the above scaling result.

It would now appear to be straightforward to improve the agreement between the series expansion solutions and the 'exact' numerical results by taking into account that both the shrinkage rate and the characteristic time itself are functions of time, i.e. by considering the next terms in the series expansions (18) and (25). This leads to

$$t_c = \frac{\pi + \cosh^{-1}(3)}{8\sqrt{2\pi}} + \pi \frac{\pi + \cosh^{-1}(3) - 2\sqrt{2}}{4\sqrt{2}\,Re} t + O\left(\frac{t^2}{Re^2}\right). \tag{40}$$

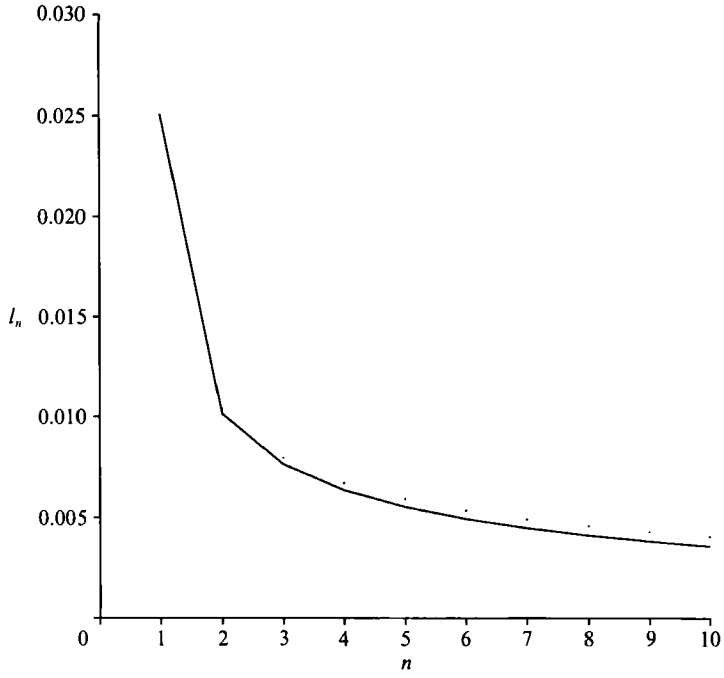

FIGURE 8. A comparison between the scaling result (39) (curve) and numerical results (dots) for the interval sizes $l_n(n)$ for $Re = 1000$. The proportionality constant has been selected such that the two data sets agree for l_1.

This expression indicates that the duration of shedding cycles grows in time, as the characteristic velocity u_c decreases more rapidly than the perimeter half-length. However, as figure 9 shows, this is in contrast to the results of numerical simulations discussed in more detail below, which show that the difference between the escape times of successive intervals in general decreases. The reason for this discrepancy lies in the fact that the choice of the maximum velocity occurring along the separatrix as the characteristic velocity has serious shortcomings. Just before a particle leaves the interior of the cat's eye, it spends most of its time near the stagnation point in a region of very small velocities, i.e. velocities significantly different from our choice of u_c. Since u_c does not account for this effect, we cannot base the calculation of improved characteristic times on it. The fact that u_c still leads to the correct functional dependency of l_1 on Re is not surprising if we realize that any constant would have given us the proper functional form. We will present an alternate way to compute the escape time for particles in l_1 in §5; however, the extension to subsequent intervals is not straightforward. We have been unable to obtain an accurate expression for the $O(t/Re)$ term in the expansion for t_c and thus develop a better concept for establishing characteristic times leading to improved estimates for more than one shedding cycle. However, in Appendix C we will outline how the next term in the expansion for t_c, were it available, could be employed to obtain improved results for l_n.

From figure 8, we recognize that the length l_n of an interval decreases as n increases, which means that with each half-cycle a smaller and smaller amount of fluid leaks out of the cat's eye. l_n will have to asymptotically approach zero, as the width of the cat's eye tends to zero only for infinite time. The amount of fluid left within the cat's eye and the flux across the separatrix at time t can easily be

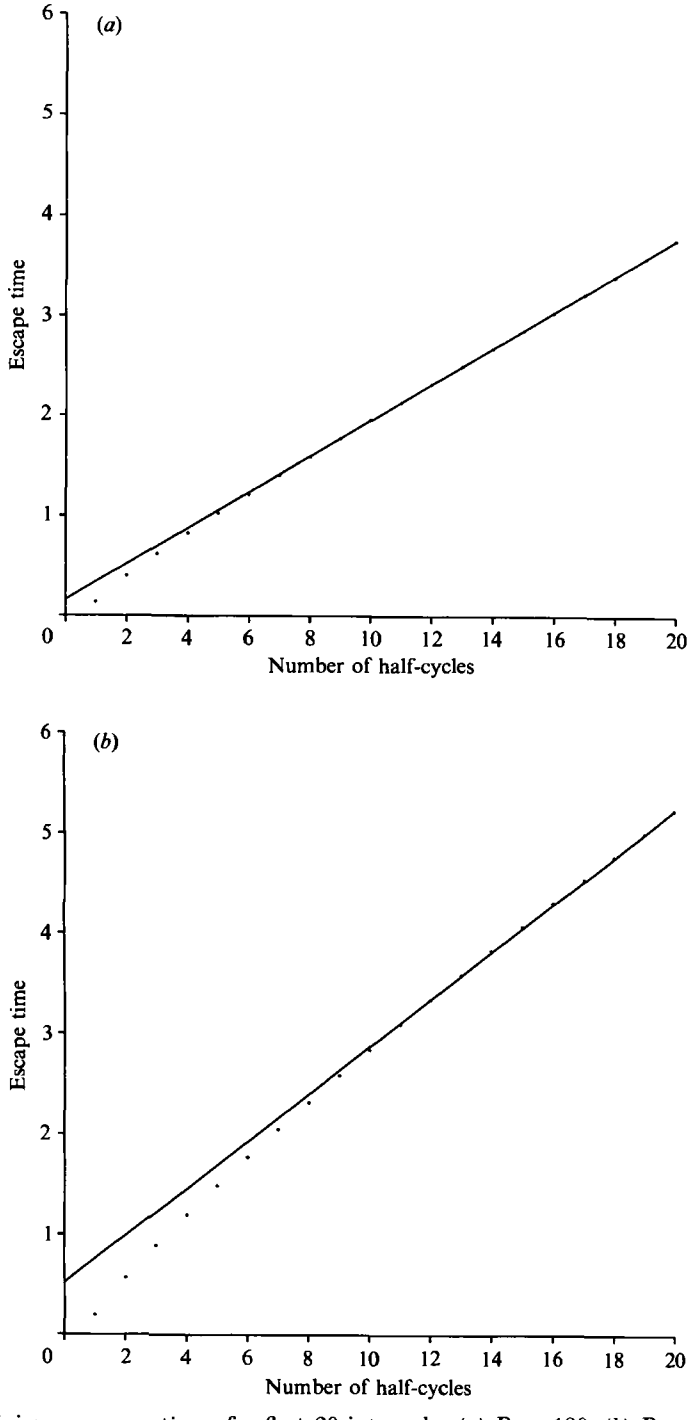

FIGURE 9. Minimum escape times for first 20 intervals: (*a*) $Re = 100$, (*b*) $Re = 1000$. Notice that after an initial transient, during which the growth of the escape times slows down, the minimum escape times increase linearly with the interval number.

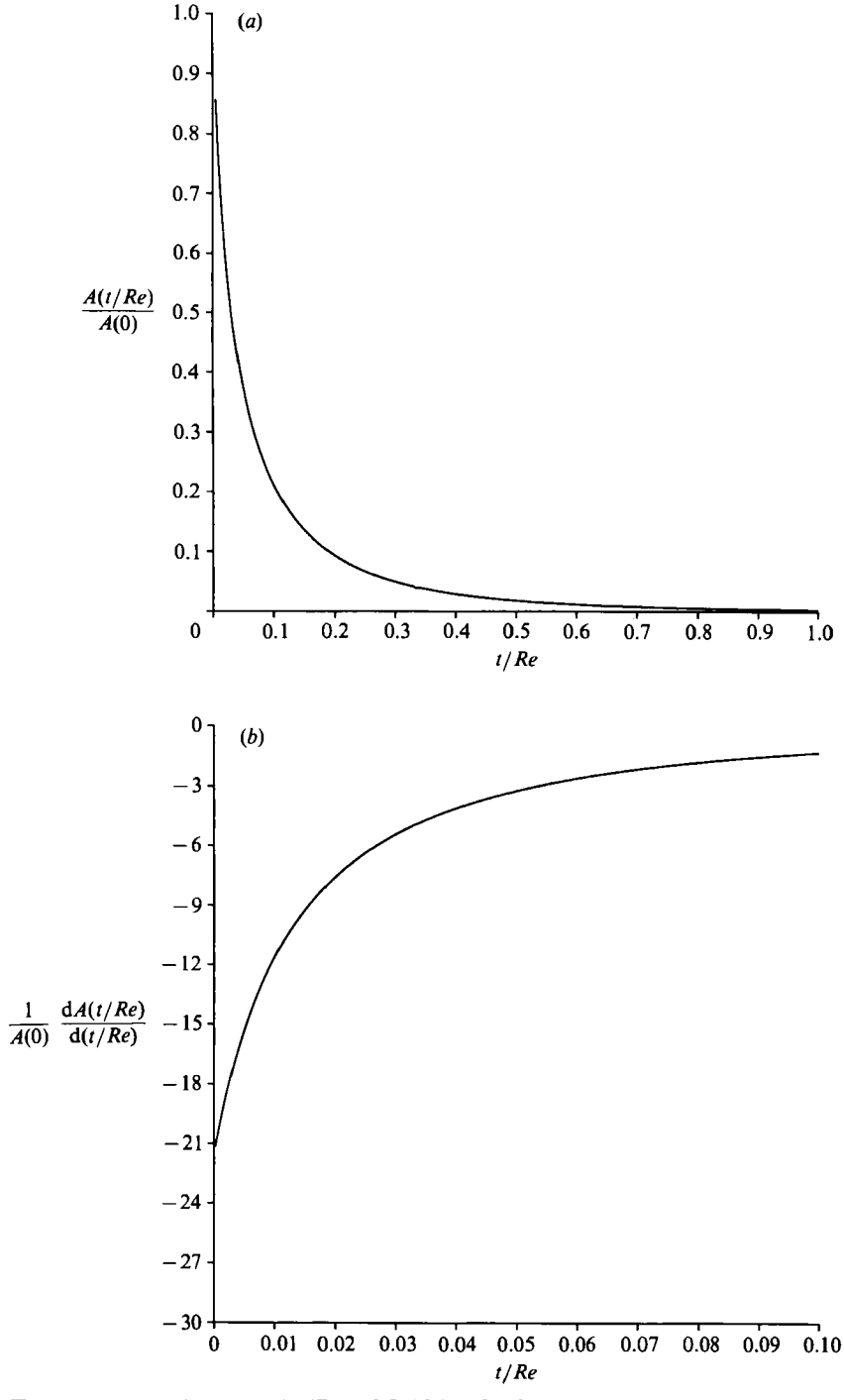

FIGURE 10. (*a*) Amount $A(t/Re)$ of fluid inside the cat's eye normalized by $A(0)$. The monotonic decrease of $A(t/Re)/A(0)$ in time corresponds to less and less fluid trapped by the cat's eye. (*b*) Flux $\mathrm{d}A/\mathrm{d}(t/Re)$ across the separatrix normalized by $A(0)$.

evaluated. This second quantity is helpful in characterizing the mixing of the fluids. From (20) we obtain for the shape of the separatrix

$$y(x) = \frac{1}{2\pi}\cosh^{-1}[1+\rho+\rho\cos(2\pi x)] \tag{41}$$

so that the area A of the cat's eye depends on ρ as

$$A(\rho) = \frac{2}{\pi}\int_0^{\frac{1}{2}} \cosh^{-1}[1+\rho+\rho\cos(2\pi x)]\,\mathrm{d}x. \tag{42}$$

With (10) we find that

$$A\left(\frac{t}{Re}\right) = \frac{2}{\pi}\int_0^{\frac{1}{2}} \cosh^{-1}\left[1+\frac{1+\cos(2\pi x)}{\cosh\left[2\pi\left(\frac{4t}{Re}\right)^{\frac{1}{2}}\right]}\right]\mathrm{d}x. \tag{43}$$

Figure 10(*a*) shows how $A(t/Re)/A(0)$ approaches zero as t/Re increases. The flux across the separatrix $\mathrm{d}A/\mathrm{d}(t/Re)$ normalized by $A(0)$ is given by

$$\frac{\mathrm{d}A\Big/\left[\mathrm{d}\left(\frac{t}{Re}\right)\right]}{A(0)} = -\frac{2\pi}{\left(\frac{t}{Re}\right)^{\frac{1}{2}}\int_0^{\frac{1}{2}} f(0,x)\,\mathrm{d}x\cosh^2\left(4\pi\left(\frac{t}{Re}\right)^{\frac{1}{2}}\right)}\frac{\sinh\left(4\pi\left(\frac{t}{Re}\right)^{\frac{1}{2}}\right)}{}\int_0^{\frac{1}{2}}\frac{1+\cos(2\pi x)}{\sinh\left[f\left(\frac{t}{Re},x\right)\right]}\mathrm{d}x, \tag{44}$$

where $f(t/Re, x)$ is

$$f\left(\frac{t}{Re},x\right) = \cosh^{-1}\left[1+\frac{1+\cos(2\pi x)}{\cosh\left[2\pi\left(\frac{4t}{Re}\right)^{\frac{1}{2}}\right]}\right]. \tag{45}$$

Figure 10(*b*) shows the flux as a function of time, normalized by $A(0)$.

5. Escape times

For the present flow field, we will analyse two different mixing events: how the fluid within the cat's eye is mixed with the fluid outside, and how the fluid initially in the top half of the cat's eye mixes with that in the bottom half. The crucial parameter characterizing the efficiency of the mixing process is the rate at which interfacial area is generated. This, in turn, depends on two different mechanisms: first, on the rate at which new lobes of fluid emerging from the cat's eye are being formed (corresponding to the escape layers discussed in §4), and second, on the rate at which the interface of each lobe is stretched. The local rate of interface stretching, especially during the early stages of the lobe's existence, is intimately linked to the escape times of the particles forming the lobe's interface. The reason for this lies in the fact that, within a given interval l_i, the escape time of a particle varies from a minimum value for a particle placed somewhere in the interior of the interval, to infinity for a particle placed at the interval endpoints. Hence, in this section we will analyse the escape times of the particles distributed along an interval. We define the time of emergence of lobe i as the time at which the first particle from interval l_i escapes from the cat's eye, i.e. is located outside the separatrix. We will analyse the formation of the first lobe in detail before proceeding to the emergence of subsequent lobes.

5.1. *Formation of the first lobe*

Figure 11 shows the numerically obtained escape times of particles distributed along l_1 for Reynolds numbers of 100 and 1000. The most striking feature lies in the fact that for each Re most particles escape from the cat's eye at essentially one time level, i.e. in the plot of escape time *vs.* initial location a plateau exists, stretching from $x = -\frac{1}{2}$ to near the opposite end of l_1. This observation of the nearly simultaneous escape of the bulk of particles leads us to the conclusion that at this particular time the material line element formed by the particles initially distributed along the interval l_1 is almost identical to the instantaneous separatrix near $x = -\frac{1}{2}$. On this basis, we can calculate the escape time for l_1 as a function of the Reynolds number, since it is given by the time at which the slope of the separatrix equals the slope of the line of marker particles near the left stagnation point. With (41) for the cat's eye's separatrix, we obtain for its slope

$$\frac{\mathrm{d}y}{\mathrm{d}x} = -\frac{\rho \sin(2\pi x)}{((1+\rho+\rho\cos(2\pi x))^2-1)^{\frac{1}{2}}}. \tag{46}$$

While the slope is, of course, not defined at the stagnation point $(-\frac{1}{2}, 0)$ itself, we can expand the right-hand side to obtain the slope near $x = -\frac{1}{2}$. By introducing $x' = x+\frac{1}{2}$ and considering only the leading order terms, we find

$$\frac{\mathrm{d}y}{\mathrm{d}x'} = \frac{\rho(2\pi x' - \ldots)}{((1+\rho-\rho(1-2\pi^2 x'^2+\ldots))^2-1)^{\frac{1}{2}}} \tag{47}$$

which yields

$$\frac{\mathrm{d}y}{\mathrm{d}x} = \rho^{\frac{1}{2}} \tag{48}$$

near the stagnation point. Since ρ depends on time as shown in §2, this expression is consistent with the known slopes of the separatrix at $t = 0, \mathrm{d}y/\mathrm{d}x = 1$, and $t \to \infty$, $\mathrm{d}y/\mathrm{d}x \to 0$.

As a next step, we have to find the slope of the material line of marker particles. Keeping in mind that the stagnation point will for all times remain part of that material line, we can calculate its slope as that of the straight line between the stagnation point and the position (x_1', y_1') of a particle initially located at $(-\frac{1}{2}+\epsilon, 0)$. For this purpose, we consider the velocity field around the stagnation point as time independent, so that we can write for (x_1', y_1')

$$x_1' = \epsilon + \int_0^t u(x_1', y_1')\,\mathrm{d}t, \tag{49}$$

$$y_1' = \int_0^t v(x_1', y_1')\,\mathrm{d}t, \tag{50}$$

where we again use the coordinates $x' = x+\frac{1}{2}, y' = y$. Close to the stagnation point the velocity field has the form $u = Ay', v = Ax'$. For the flow field under consideration, the stream function (3) leads to

$$A = \frac{4\pi^2\rho}{1+\rho}, \tag{51}$$

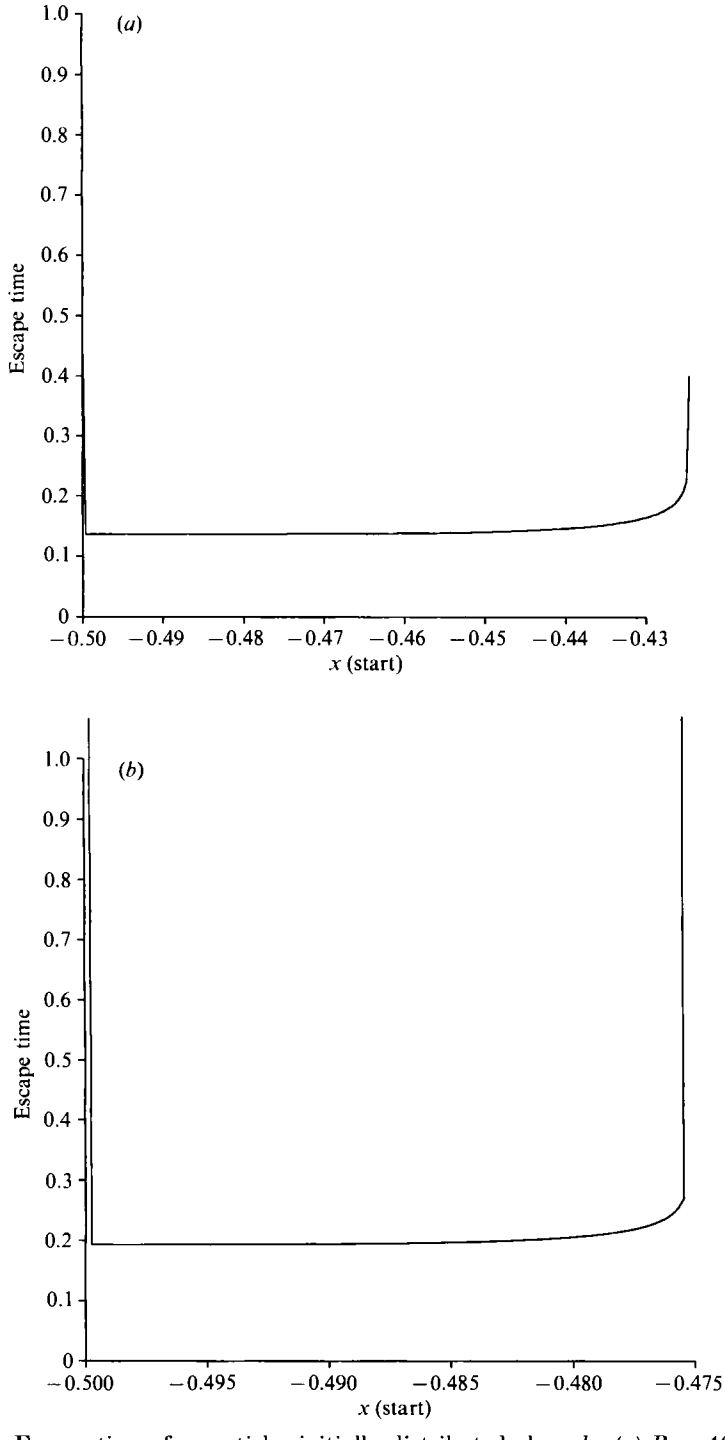

FIGURE 11. Escape times for particles initially distributed along l_1: (*a*) $Re = 100$, (*b*) $Re = 1000$. Notice the existence of a plateau value indicating that most particles escape from the cat's eye at the same time. Based on this observation, we can approximately calculate the plateau time.

so that for $t = 0$, i.e. $\rho = 1$, we obtain

$$u = 2\pi^2 y', \tag{52}$$

$$v = 2\pi^2 x'. \tag{53}$$

From this we get the position of a marker particle:

$$x_1'(t) = C_1 e^{2\pi^2 t} + C_2 e^{-2\pi^2 t}, \tag{54}$$

$$y_1'(t) = C_1 e^{2\pi^2 t} - C_2 e^{-2\pi^2 t}. \tag{55}$$

From the initial conditions $x_1'(0) = \epsilon, y_1'(0) = 0$, the constants are given by $C_1 = C_2 = \frac{1}{2}\epsilon$. The slope of the material line can then be evaluated and is given by

$$\frac{y_1'(t)}{x_1'(t)} = \frac{e^{2\pi^2 t} - e^{-2\pi^2 t}}{e^{2\pi^2 t} + e^{-2\pi^2 t}} = \tanh(2\pi^2 t). \tag{56}$$

We note that this expression for the slope of the material line is valid for all times in the case of a time-dependent velocity field. The escape time is now given by

$$\tanh(2\pi^2 t) = \rho^{\frac{1}{2}} = \frac{1}{\left(\cosh\left[2\pi\left(\frac{4t}{Re}\right)^{\frac{1}{2}}\right]\right)^{\frac{1}{2}}}. \tag{57}$$

which, for small t/Re, we can expand:

$$\tanh(2\pi^2 t) = 1 - \frac{4\pi^2 t}{Re} + O\left(\left(\frac{t}{Re}\right)^2\right). \tag{58}$$

As t itself is not necessarily small, we cannot expand the left-hand side to obtain an explicit equation for t. However, an iterative numerical solution of (57) gives $t_{esc}(Re = 100) \sim 0.10$, and $t_{esc}(Re = 1000) \sim 0.15$. These results are in reasonable agreement with figure 11. More important, they show the correct behaviour of increasing escape time with increasing Re. The quantitative error is due to the assumption of a time-independent velocity field.

5.2. *Formation of subsequent lobes*

Figure 12 presents the escape times of particles distributed over the first ten intervals l_1 to l_{10} for Re of 100 and 1000. We recognize that, except for the first interval, the escape times do not exhibit the plateau-like behaviour described above. The obvious reason lies in the fact that for $i > 1$ the marker particles representing l_i are not aligned with x-axis at the beginning of the half-cycle during which they will escape from the cat's eye. Hence, there will not be a time at which the material line element represented by these particles collapses with the instantaneous separatrix, as was the case for l_1. Consequently, the concept for calculating escape times presented in the previous section cannot be extended beyond l_1. We notice that, as i increases, the part of l_i closer to the centre of the cat's eye tends to escape earlier than the region of l_i closer to the stagnation point. This reflects the slowdown experienced by particles as they pass closely by the stagnation point. Comparison of the results for $Re = 100$ and $Re = 1000$ confirms the scaling of the interval size with Re in the manner discussed in §4. We furthermore see that the minimal escape times for each interval increase at a slower rate for $Re = 100$ than for $Re = 1000$. Figure 9 shows the minimal escape time as a function of the interval number. After an initial transient period, the escape time depends linearly on the interval number. The transient period

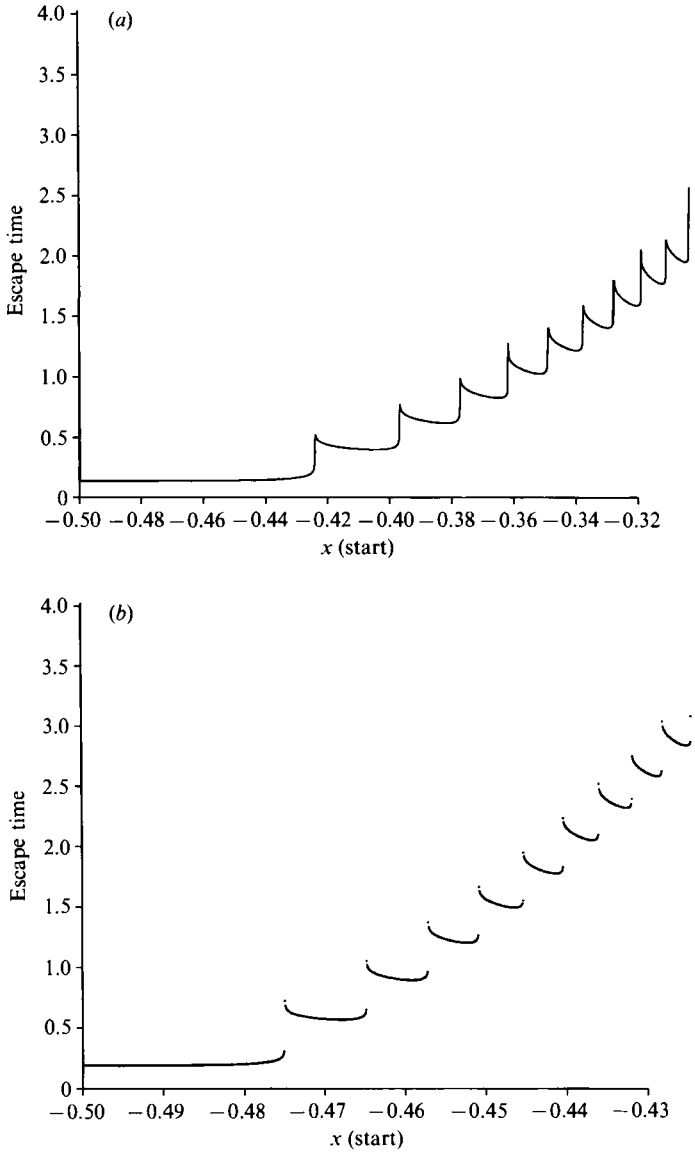

FIGURE 12. Escape times for particles initially distributed along the first ten intervals l_1 to l_{10}: (*a*) $Re = 100$, (*b*) $Re = 1000$. While we observe the existence of a plateau for l_1 as discussed above, such plateaux do not exist for subsequent intervals. Notice the sharp increase of the particle escape times near the borders between two adjacent intervals. A particle initially located exactly on the border between adjacent intervals will stay within the cat's eye for infinitely long times.

lasts longer for the higher value of Re. This linear behaviour represents an *a posteriori* justification for estimating the l_n in §4 on the basis of a constant characteristic time, and it explains why this estimate proved to be fairly accurate.

5.3. *Self-similarity in the lobe formation process*

In this section, we will focus our attention on the small region around the border between l_1 and l_2, and on how a particle's escape time depends on its starting position in this region. Figure 13(*a*) shows a blow-up of this region for $Re = 1000$. In figure

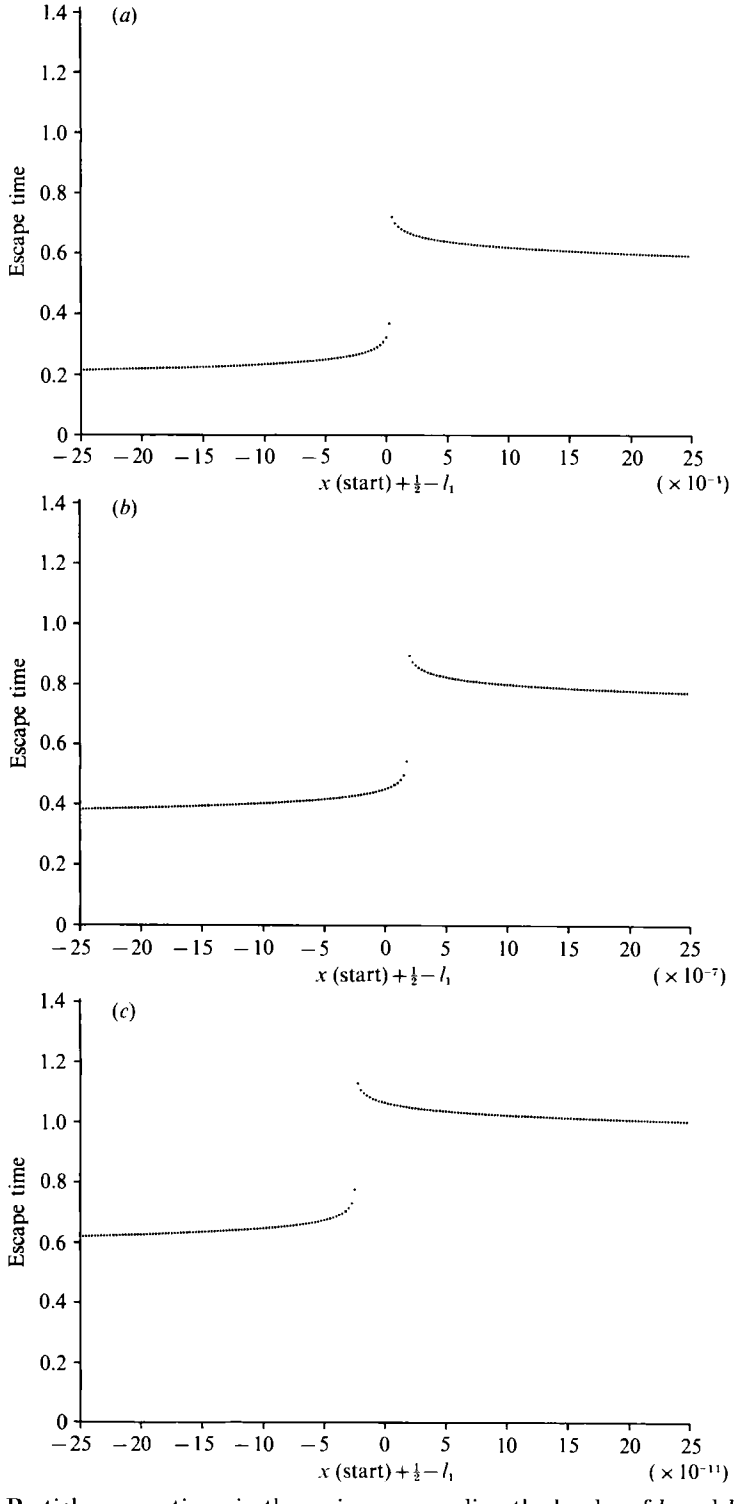

FIGURE 13. Particle escape times in the region surrounding the border of l_1 and l_2 for $Re = 1000$. Observe the self-similar blow-up of the escape times as we focus on a smaller and smaller region next to the border. The horizontal scale in (*b*) has been stretched by a factor of 1000 compared with (*a*), and in (*c*) by a further 10000.

13(*b*) the horizontal scale has been stretched by a factor of 1000, and in figure 13(*c*) by another factor of 10000. We recognize that the particle escape time increases in a self-similar fashion as we approach the boundary between l_1 and l_2. In order to explain this behaviour of the real flow, we will study the simplified generic problem of flow near a stagnation point as sketched in figure 14 in the coordinate system x', y'. Close to the stagnation point, the velocity field is given by

$$u = -\Lambda x', \tag{59}$$

$$v = \Lambda y'. \tag{60}$$

This coordinate system is not related to the system x', y' used above. The stream function ψ' has the form

$$\psi'(x', y') = -\Lambda x' y'. \tag{61}$$

As a result, streamlines are given by

$$y' = -\frac{y'_{\text{ref}}}{x'}, \tag{62}$$

where y'_{ref} represents the y'-coordinate of the streamline at $x' = -1$, where the particle is assumed to be at $t = 0$. We now proceed to find the position at which a particle path intersects the separatrix, upon which we can determine the time at which the particle crosses the separatrix, i.e. the particle escape time. As a first approximation, we assume the velocity field to be time independent, whereas in the full problem both the streamlines and the separatrix change with time. Consequently, the particle paths are identical to the streamlines and given by (62) near the stagnation point. We can assume the separatrix to be a straight line near the stagnation point

$$y' = -bx' \tag{63}$$

so that we obtain the y'-coordinate of the point of intersection as

$$y'_{\text{int}} = (y'_{\text{ref}} b)^{\frac{1}{2}}. \tag{64}$$

Since v is a function of y' only, we can now determine the time it takes a particle to travel from y'_{ref} to the escape point y'_{int} as

$$t_{\text{esc}} = \int_{y'_{\text{ref}}}^{y'_{\text{int}}} \frac{\mathrm{d}y'}{v} = \int_{y'_{\text{ref}}}^{y'_{\text{int}}} \frac{\mathrm{d}y'}{\Lambda y'} = \frac{1}{\Lambda} \ln \frac{y'_{int}}{y'_{ref}}. \tag{65}$$

With (64) we obtain

$$t_{\text{esc}} = \frac{1}{\Lambda} \ln \left(\frac{b}{y'_{\text{ref}}} \right)^{\frac{1}{2}} = \frac{1}{2\Lambda} \ln b - \frac{1}{2\Lambda} \ln y'_{\text{ref}}. \tag{66}$$

We can now translate this analysis to the original problem by interpreting y'_{ref} as the small distance between a particle starting position and the border between l_1 and l_2. We thus recognize that the cat's eye flow field gives rise to the self-similar logarithmic blow-up of the escape time as shown in figure 13(*a–c*).

We furthermore observe that if we plot the x-component of the escape location as a function of $(x+\frac{1}{2})/l_1$, we obtain identical curves for $Re = 100$ and $Re = 1000$ (figure

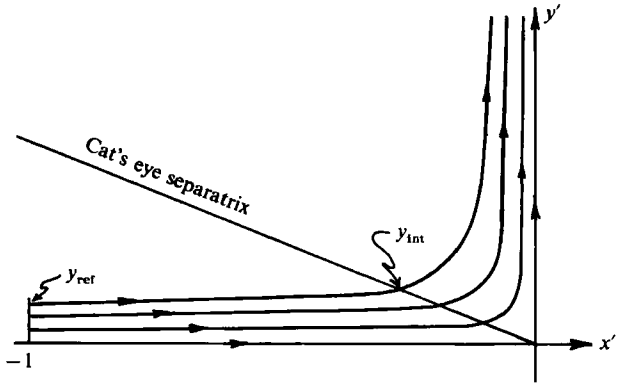

FIGURE 14. Sketch of generic stagnation point flow employed to explain the self-similar blow-up of the escape times near the interval borders.

15). This implies that as we vary Re, the evolution of the separatrix and the material line element do not change independently from each other. Rather, the separatrix and the material line element are affected by Re in such a way that a particle released at $(x+\frac{1}{2})/l_1$ escapes from the cat's eye at the same x-location, independent of the Reynolds number.

6. Mixing

In this section, we will focus our attention on the generation of interfacial area, which is essential for the efficiency of the mixing process. As mentioned above, we are interested in two different mixing processes: the mixing of the fluid inside the cat's eye with that outside of it, and the mixing of the fluid initially in the top half of the cat's eye with that in the bottom half. For this purpose, we have performed a numerical simulation of the full problem, the results of which are depicted in figure 16. We consider the fluid that is initially located between the separatrix and the streamline that intersects the x-axis at the border between l_4 and l_5. We track the fluid by placing several hundred marker particles along its envelope at time $t = 0$ and computing their trajectories by means of a Runge–Kutta time integration scheme. The fraction of this fluid initially located in the top half of the cat's eye is depicted as black, that in the bottom half as white. The reason for not simply considering the full top and bottom of the cat's eye halves is that the interface between the two would pass through the initial point-vortex singularity, thus causing numerical problems due to infinite velocities. Hence we mark the inner region of the cat's eye as cross-hatched, and the numerical simulation will reveal the evolution of its outer boundary. We observe that at time $t = 0.101$ bulges of black and white fluid, respectively, are forming near the stagnation points. Those fluid regions initially closer to the centre of the cat's eye, however, have already left the stagnation-point region and are on their way to the opposite stagnation point. At $t = 0.201$, a first lobe of escaping fluid is visible near each of the stagnation points, and patches of fluid of opposite colour are now beginning to form next to them. These patches have begun to escape by $t = 0.301$, while the first pair of lobes has been stretched out to a thin filament, primarily under the action of the strain field outside of the cat's eye and near the stagnation point. At $t = 0.401$, new patches of fluid of the same colour as the first lobe are forming near the stagnation points. Meanwhile, the previous lobes have formed thin filaments within the filaments from the first escaping lobes. At $t = 0.501$,

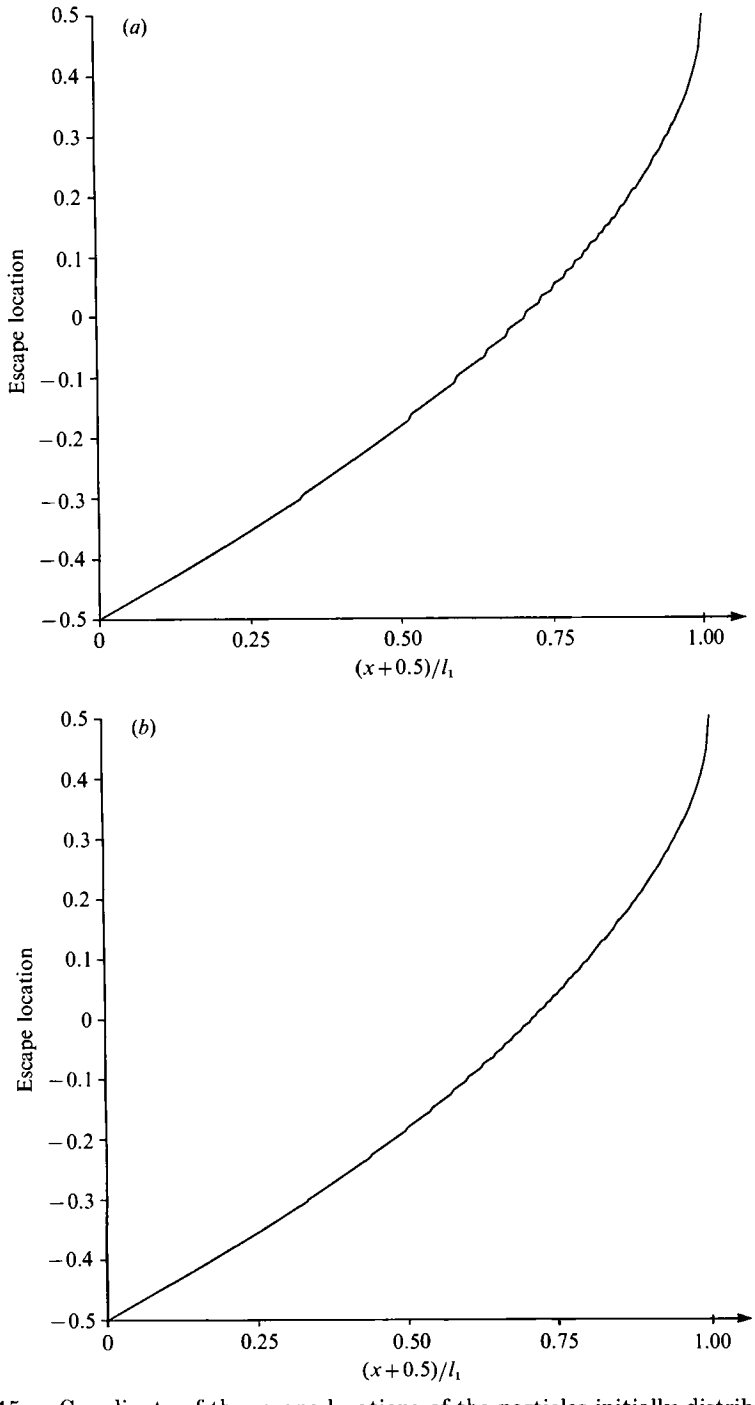

FIGURE 15. x-Coordinate of the escape locations of the particles initially distributed along l_1: (*a*) $Re = 100$, (*b*) $Re = 1000$. The two curves are almost identical, indicating that the evolution of the separatrix and the material line element occurs in a coupled fashion as we vary Re.

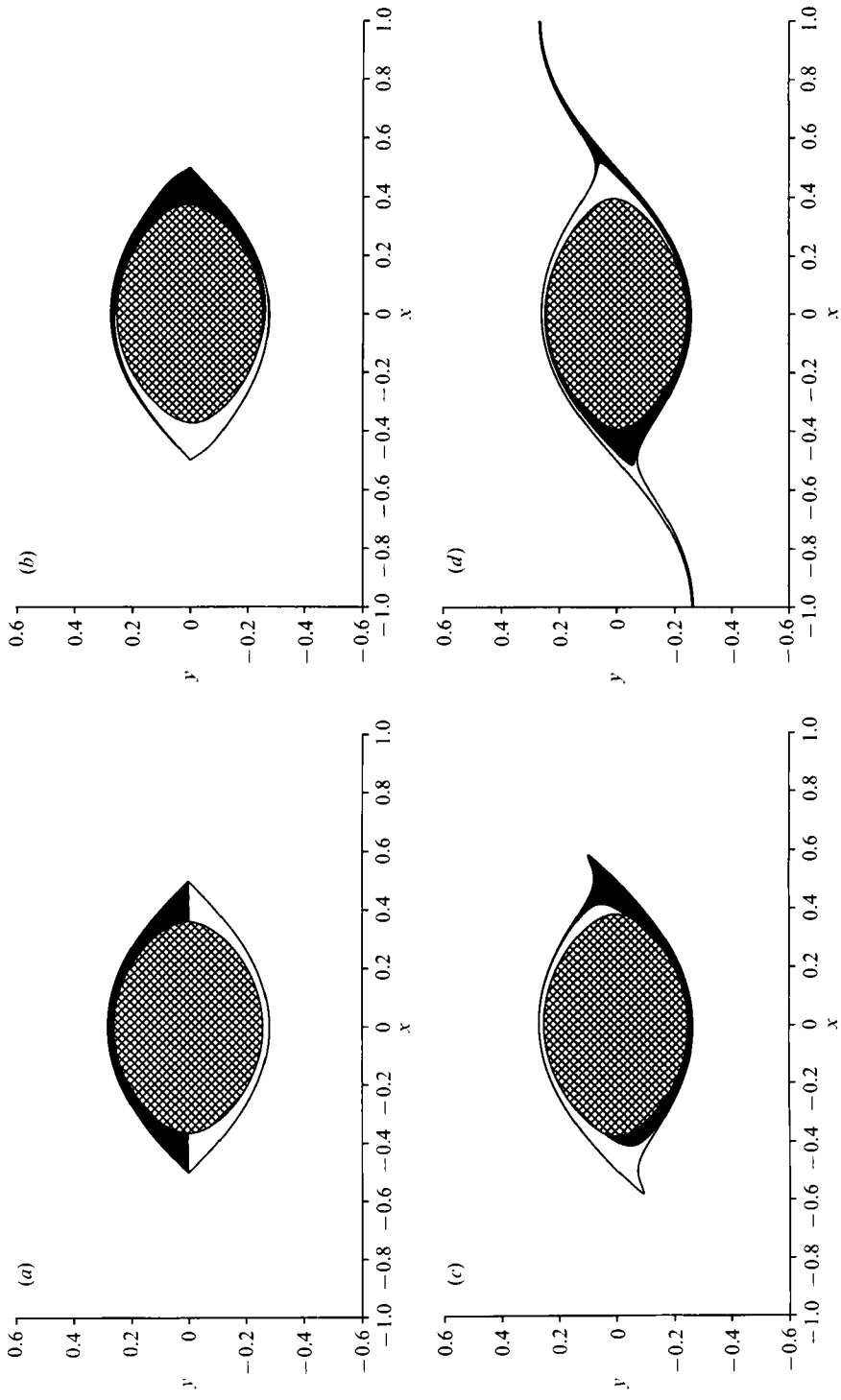
(a)
(b)
(c)
(d)
y
x
0.6
0.4
0.2
0
−0.2
−0.4
−0.6
−1.0
−0.8
−0.6
−0.4
−0.2
0
0.2
0.4
0.6
0.8
1.0

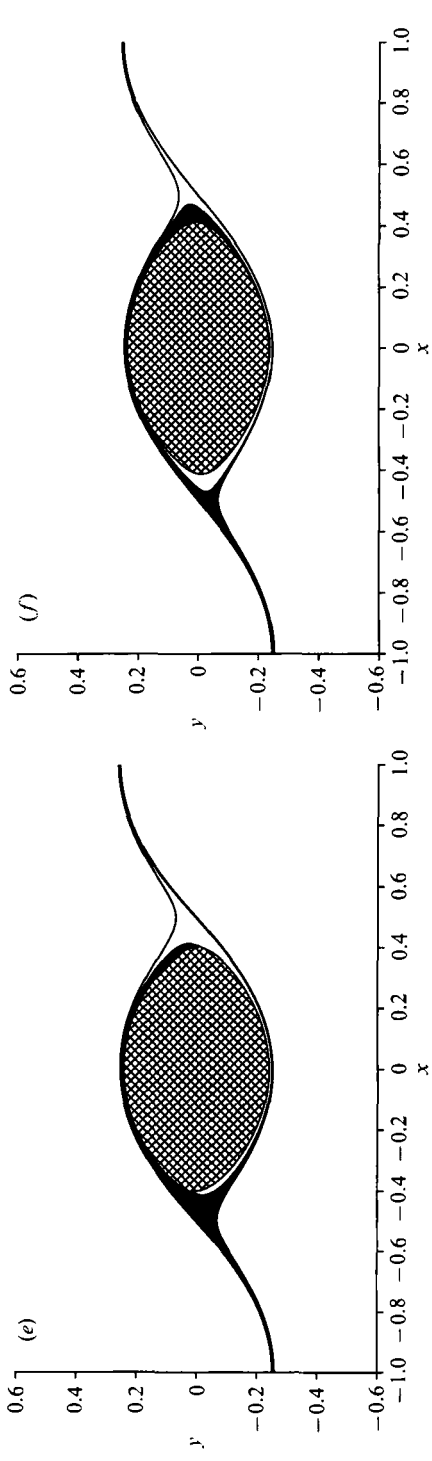

FIGURE 16. Numerical simulation of the mixing of different fluid regions for $Re = 100$. Shown are the times 0.001, 0.101, 0.201, 0.301, 0.401, 0.501, 0.601, and 0.701. (*a–h*) respectively. We observe the formation of fluid lobes or filaments as the fluid escapes from the cat's eye. Notice that, for example, patches of the fluid marked in black alternatingly escape to the upper right and the lower left, thus resulting in strong interfacial growth.

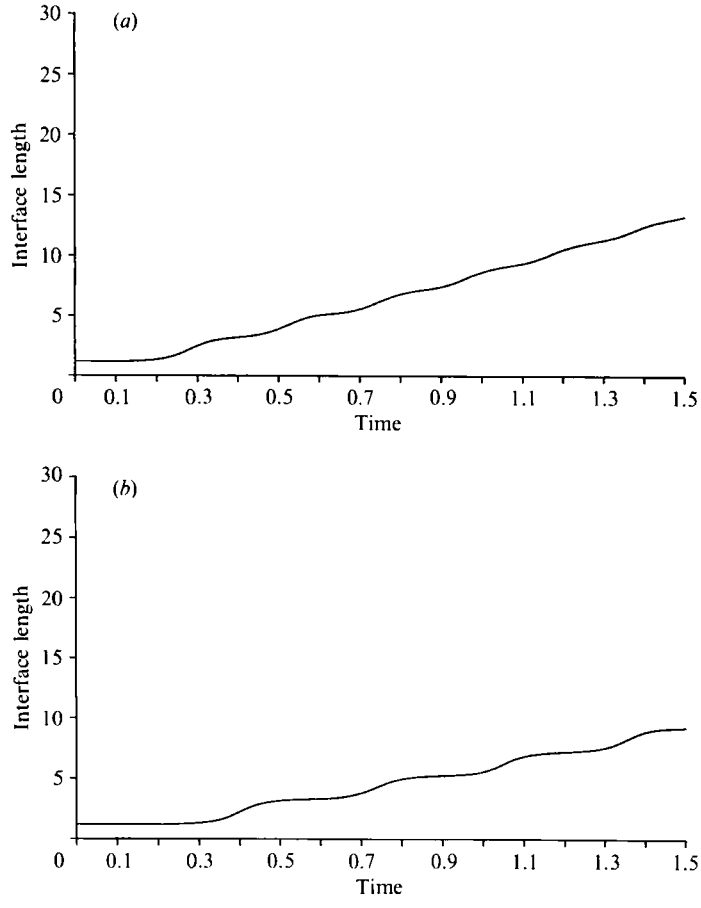

FIGURE 17. Growth of the interfacial length between the black fluid initially trapped within the cat's eye and the fluid outside. While the interface would not grow for inviscid flow, viscosity and the related effect of fluid leakage lead to an interfacial growth approximately proportional to time: (*a*) $Re = 100$, (*b*) $Re = 1000$.

0.601, and 0.701, we see parts of the new patches escape, while the rest of them travel on to the opposite stagnation point.

The picture that emerges from this simulation is that, through a process of stretching and folding, lobe after lobe forms and subsequently is being stretched out into a thin filament. As a result, small-scale striations develop near the stagnation points and in the regions outside the cat's eye. The cross-hatched region marking the fluid initially at the centre of the cat's eye shrinks in the transverse direction while expanding in the streamline direction. If we were to continue this simulation, we would soon see the first of the cross-hatched fluid escaping near the stagnation point.

We can now estimate the rate at which interfacial area is being generated between the fluid that initially resides within the cat's eye and that outside. The dominant factor determining the total interfacial area is the formation of the thin filamented lobes of escaping fluid. Consequently, the interfacial growth rate should be nearly proportional to the speed of the tip of the filament. If, to a first approximation, we consider the velocity field as time-independent, the velocity of the tip will perform a periodic oscillation in time as it passes by cat's eye after cat's eye. Since the path length that the tip traverses across each cat's eye is identical, the total interfacial

area should grow approximately linearly in time, which is confirmed by the numerical results presented in figure 17. This is in contrast to the inviscid flow, in which no fluid escapes from the cat's eye, so that the total interfacial area is not a function of time. As a result, we notice that for the flow under consideration, viscosity leads to a growth proportional to time of the interface between the fluid inside and that outside of the cat's eye. Figure 17 furthermore shows that for $Re = 100$ the proportional factor is larger than for $Re = 1000$, which does not come as a surprise as lobes form at a faster rate for $Re = 100$.

For the case of interface generation between the fluid initially in the upper half and that initially in the lower half of the cat's eye, the situation is a slightly different one. Even for the time-independent inviscid velocity field, the interface grows linearly in time (figure 18). If we let the cat's eye evolve in time under the action of viscosity, the interface grows more rapidly. We can estimate this rate of growth by realizing that the interfacial length depends on the length of the evolving filaments, as within each filament we have a thinner filament of opposite fluid. Furthermore, it depends on the number of evolving filaments, i.e. the rate at which lobes escape. Since we noticed above that each filament grows approximately linearly in time, and since we showed in §5 that, after an initial transient, the number of lobes grows linearly in time as well, we expect the total interface to grow approximately quadratically in time, which is confirmed by the numerical simulation (figure 18). Again, viscosity adds a factor of t to the growth rate of the interface.

7. Summary and conclusion

The present paper represents a study of fluid mixing in a row of viscously diffusing point vortices. Our model is based on Stuart's one-parameter family of solutions to the steady Euler equations. We relate the free parameter to the core size of the vortices, which we subsequently let grow according to the exact solution of the Navier–Stokes equations for an isolated diffusing point vortex. While we do not have an exact solution for a row of viscously diffusing point vortices, our model approaches that solution for small values of t/Re. In comparison with a numerical solution of the Navier–Stokes equations (which would be hard to obtain owing to the initial singularity), the current approach allows us to investigate some aspects of the flow analytically. In particular, we have focused on a description of how the shrinking of the cat's eye is related to fluid leaking out of the trapped region into the free streams. We observe that fluid from neighbouring intervals in the cat's eye escapes in opposite directions, thus giving rise to an infinite number of lobes or filaments. The size of these intervals l_n scales with the inverse square root of the Reynolds number and depends on n. These results have been confirmed numerically. We furthermore observe the existence of a plateau in the escape time for the particles located within l_1, which allows us to derive a general relationship describing the escape time as a function of the Reynolds number. However, this approach is valid only for the first interval. We furthermore observe a self-similar blow-up of the escape time for the particles near the border between two adjacent intervals, which can be explained on the basis of a simple stagnation-point flow.

When analysing the interface generation or stretching rate between the fluid initially trapped inside the cat's eye and that outside, we notice that viscosity leads to an interface growth proportional to t. For the interfacial area separating the fluid in the top half of the cat's eye from that in the bottom half, viscosity is shown to lead to an increase in the growth rate from $O(t)$ to $O(t^2)$. Thus, and this represents the

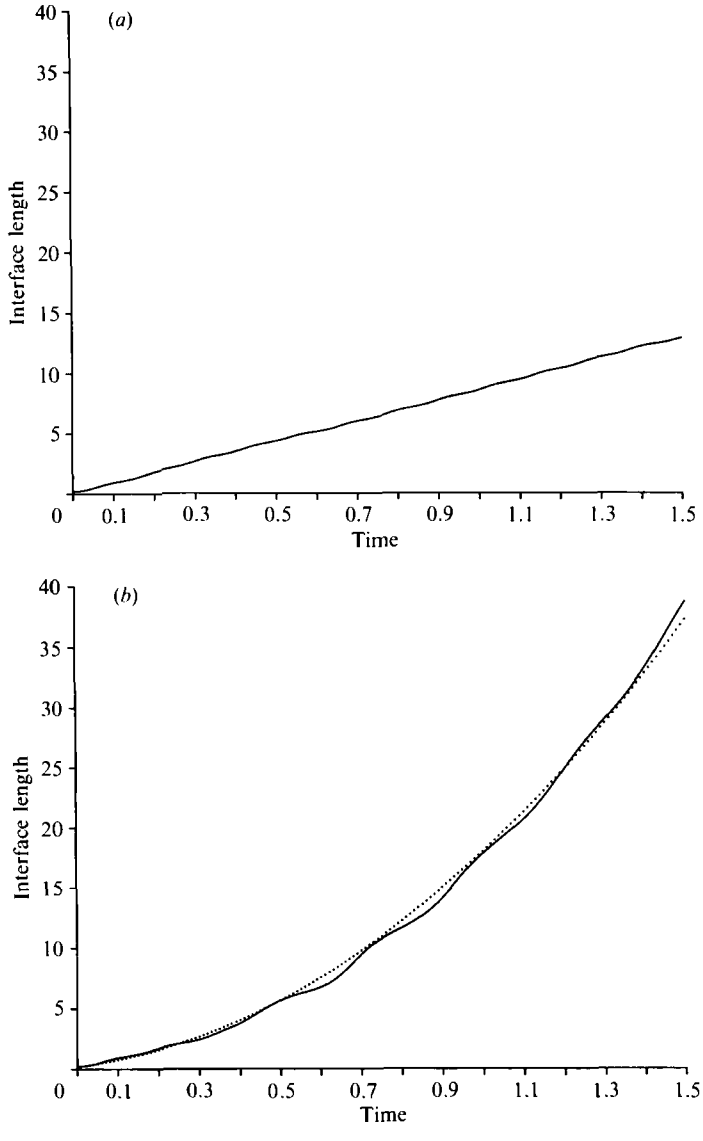

FIGURE 18(*a*, *b*). For caption see facing page.

central conclusion of the present study, viscosity fundamentally changes the flow as far as mixing is concerned, by leading to an additional factor of t in the interface growth rate for both cases investigated. This is perhaps somewhat surprising as in the previously mentioned studies of chaotic advection the stretching rate is typically exponential.

A logical extension of the current work will have to include dynamical effects of the vortices as well, i.e. the tendency of the row of vortices to become unstable and undergo a pairing process. This step is expected to significantly change the underlying mixing processes and affect the interfacial growth rates, and it is hoped to result in a better understanding of the evolving small-scale structures and entrainment processes. In addition, we believe that the results presented here should

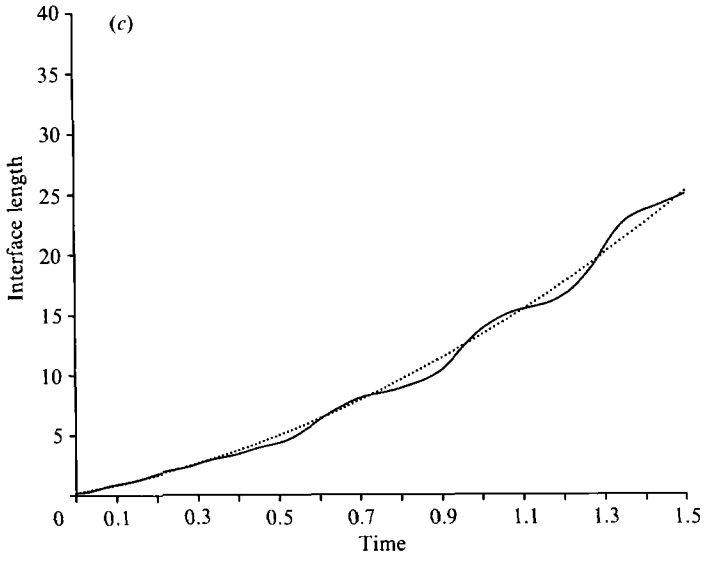

FIGURE 18. Generation of interfacial length between the black and white fluid regions. While the interface grows linearly in time for the inviscid case (*a*), the formation of fluid filaments due to viscosity leads to interface growth rates of $O(t^2)$: (*b*) $Re = 100$, (*c*) $Re = 1000$ (the dotted curve is a parabolic fit).

be applicable to other configurations such as the Kármán vortex street or plane jets idealized by diffusive point vortices.

We gratefully acknowledge several helpful discussions with Professor J. T. Stuart, as well as a useful discussion with Professor A. Tzavaras. This research was largely performed during a visit of P.K.N. to the Center for Fluid Mechanics at Brown University. Funding was provided by DARPA under URI contract no. N00014-86-K0754 (to Brown University), by the National Science Foundation under grant no. MSM-8809438 (to E.M), and by the Air Force Office of Scientific Research under grant no. AFOSR 88-0185 (to P.K.N). Supercomputing time was provided by the San Diego Supercomputer Center.

Appendix A. Error between model and exact solution

In the vorticity–stream-function formulation, the two-dimensional Navier–Stokes equation and the continuity equation are

$$\omega_t + \psi_y \omega_x - \psi_x \omega_y = \nu \nabla^2 \omega, \tag{A 1}$$

$$\nabla^2 \psi = -\omega. \tag{A 2}$$

Since the stream function (3) with our model assumption (10) satisfies

$$\psi_y \omega_x - \psi_x \omega_y = 0, \tag{A 3}$$

the error $E(x, y, t)$ between our viscous model and the true solution of (A 1), (A 2) is given by the terms in (A 1) we ignored. Hence

$$E(x, y, t) = -(\omega_t - \nu \nabla^2 \omega). \tag{A 4}$$

To explicitly compute E, we denote the stream function as

$$\psi(x, y, t) = \ln[\varphi(x, y, t)] \tag{A 5}$$

where $$\varphi(x,y,t) = \cosh(2\pi y) - \rho(t)\cos(2\pi x). \tag{A 6}$$

Then the vorticity can be computed from (A 2):

$$\omega = -\nabla^2\psi = -\frac{1}{\varphi}(\nabla^2\varphi) + \left(\frac{\varphi_x}{\varphi}\right)^2 + \left(\frac{\varphi_y}{\varphi}\right)^2. \tag{A 7}$$

After some tedious algebra, this simplifies to

$$\omega = -(2\pi)^2(1-\rho^2)/\varphi^2. \tag{A 8}$$

Using this expression in (A 4) gives the following formula for the error:

$$E(x,y,t) = \frac{-2(2\pi)^2\rho\dot{\rho}}{\varphi^2} + \frac{2(2\pi)^2(1-\rho^2)\dot{\rho}\cos(2\pi x)}{\varphi^3} - \frac{2\nu(2\pi)^2(1-\rho^2)}{\varphi^4}[-(2\pi)^2(1-\rho^2) + 2(\varphi_x^2+\varphi_y^2)]. \tag{A 9}$$

Since $\varphi(0,0,0) = 0$ and $\rho(0) = 1$, the error at the vortex centre at time $t = 0$ is undefined. For all positive times, however, (A 9) gives an explicit expression for the error in the vorticity distribution at any point in the (x,y)-plane. The possibility of using this expression to choose a better $\rho(t)$ is currently being explored.

Appendix B. Short-time expansion for the half-width of the cat's eye

The half-width of the cat's eye as function of t/Re is given by (15). By expanding

$$\cosh x = 1 + \frac{x^2}{2!} + \frac{x^4}{4!} + \ldots \tag{B 1}$$

we obtain $$y_w = \frac{1}{2\pi}\cosh^{-1}\left(1 + 2 - \frac{16\pi^2 t}{Re} + \frac{320\pi^4 t^2}{3Re^2} + O\left(\frac{t^3}{Re^3}\right)\right) \tag{B 2}$$

which we can rewrite as

$$e^{2\pi y_w} + e^{-2\pi y_w} = 6 - \frac{32\pi^2 t}{Re} + \frac{640\pi^4 t^t}{3Re^2} + O\left(\frac{t^3}{Re^3}\right). \tag{B 3}$$

Expanding $$y_w = y_0 + y_1\frac{t}{Re} + y_2\frac{t^2}{Re^2} + \ldots \tag{B 4}$$

we recover $$y_w(t=0) = \frac{1}{2\pi}\cosh^{-1}(3). \tag{B 5}$$

Comparison of the $O(t/Re)$ terms leads to

$$y_1 = -\frac{8\pi}{\sinh(2\pi y_0)}. \tag{B 6}$$

If we use the result for y_0 in this expression, we obtain

$$y_1 = -\sqrt{8\pi}. \tag{B 7}$$

The $O(t^2/Re^2)$ terms lead to

$$y_2 = \frac{22\sqrt{2\pi^3}}{3} \tag{B 8}$$

which results in the short time expansion

$$y_w = \frac{1}{2\pi}\cosh^{-1}(3) - \frac{\sqrt{8\pi}}{Re}t + \frac{22\sqrt{2\pi^3}}{3Re^2}t^2 + O\left(\frac{t^3}{Re^3}\right) \tag{B 9}$$

for the half width of the cat's eye.

Appendix C. Improved estimates for l_n

Assuming we have an expression for the characteristic time accurate to $O(t/Re)$, we can write, for the sake of brevity,

$$t_c = a + bt + O(t^2) \tag{C 1}$$

so that we get

$$\left.\begin{aligned} t_{1c} &= a, \\ t_{2c} &= a + bt_{1c} = a(1+b), \\ t_{3c} &= a + b(t_{1c} + t_{2c}) = a(1+b)^2, \\ &\vdots \\ t_{ic} &= a(1+b)^{i-1}. \end{aligned}\right\} \tag{C 2}$$

As the length of a shedding cycle varies, so does the rate at which the width of the cat's eye shrinks. From (16) we have

$$\frac{\mathrm{d}y_w}{\mathrm{d}t} = -\frac{\sqrt{8\pi}}{Re} + \frac{44\sqrt{2\pi^3}}{3Re^2}t + O(t^2). \tag{C 3}$$

By writing, again for the sake of conciseness,

$$\frac{\mathrm{d}y_w}{\mathrm{d}t} = c + et + O(t^2) \tag{C 4}$$

we obtain

$$\left.\begin{aligned} &\frac{\mathrm{d}y_w}{\mathrm{d}t}(t=0) = c, \\ &\frac{\mathrm{d}y_w}{\mathrm{d}t}(t=t_{1c}) = c + ea, \\ &\frac{\mathrm{d}y_w}{\mathrm{d}t}(t=t_{1c}+t_{2c}) = c + e(2a+ba), \\ &\vdots \\ &\frac{\mathrm{d}y_w}{\mathrm{d}t}\left(t=\sum_{j=1}^{i} t_{jc}\right) = c + \frac{ae}{b}(1+b)^{i-1} - \frac{ae}{b}. \end{aligned}\right\} \tag{C 5}$$

This allows us to compute the amount Δy_i by which the cat's eye shrinks over the duration of the ith shedding cycle

$$\Delta y_i = \frac{\mathrm{d}y_w}{\mathrm{d}t}\left(t=\sum_{j=1}^{i} t_{jc}\right) t_{ic} = \left[c - \frac{ae}{b} + \frac{ae}{b}(1+b)^{i-1}\right] a(1+b)^{i-1}. \tag{C 6}$$

As before, we employ

$$\sum_{i=1}^{n} l_i = \frac{8^{\frac{1}{4}}}{\pi^{\frac{1}{2}}}\left(\sum_{i=1}^{n} \Delta y_i\right)^{\frac{1}{2}} \tag{C 7}$$

to obtain

$$l_n = \frac{8^{\frac{1}{4}}}{\pi^{\frac{1}{2}}}\left(\left(\sum_{i=1}^{n} \Delta y_i\right)^{\frac{1}{2}} - \left(\sum_{i=1}^{n-1} \Delta y_i\right)^{\frac{1}{2}}\right) \tag{C 8}$$

where we can utilize the expression (C 6) to evaluate l_n

$$l_n = \frac{8^{\frac{1}{4}}}{\pi^{\frac{1}{2}}}\left(\left(\sum_{i=1}^{n}\left[c - \frac{ae}{b} + \frac{ae}{b}(1+b)^{i-1}\right] a(1+b)^{i-1}\right)^{\frac{1}{2}} - \left(\sum_{i=1}^{n-1}\left[c - \frac{ae}{b} + \frac{ae}{b}(1+b)^{i-1}\right] a(1+b)^{i-1}\right)^{\frac{1}{2}}\right). \tag{C 9}$$

This in turn can be simplified for $n \gg 1$ to yield

$$l_n = \frac{8^{\frac{1}{4}}}{2\pi^{\frac{1}{2}}} \frac{\Delta y_n}{\left(\sum_{i=1}^{n-1} \Delta y_i\right)^{\frac{1}{2}}}$$

$$= \frac{8^{\frac{1}{4}}}{2\sqrt{2}} \frac{[c - ae/b + ae/b(1+b)^{n-1}]\, a(1+b)^{n-1}}{\left(\sum_{i=1}^{n-1} [c - ae/b + ae/b(1+b)^{i-1}]\, a(1+b)^{i-1}\right)^{\frac{1}{2}}}. \qquad \text{(C 10)}$$

REFERENCES

Aref, H. 1984 Stirring by chaotic advection. *J. Fluid Mech.* **143**, 1–21.

Aref, H. & Balachandar, S. 1986 Chaotic advection in a Stokes flow. *Phys. Fluids* **29**, 3515–3521.

Aref, H. & Jones, S. W. 1989 Enhanced separation of diffusing particles by chaotic advection. *Phys. Fluids* A **1**, 470–474.

Arter, W. 1983 Ergodic streamlines in steady convection. *Phys. Lett.* **97** A, 171–174.

Bourland, F. J. & Haberman, R. 1990 Separatrix crossing: time invariant potentials with dissipation. *SIAM J. Appl. Maths* **50**, 1716–1744.

Broomhead, D. S. & Ryrie, S. C. 1988 Particle paths in wavy vortices. *Nonlinearity* **1**, 409–434.

Chaiken, J., Chevray, R., Tabor, M. & Tan, Q. M. 1986 Experimental study of Lagrangian turbulence in Stokes flow. *Proc. R. Soc. Lond.* A **408**, 165–174.

Dombre, T., Frisch, U., Greene, J. M., Hénon, M., Mehr, A. & Soward, A. M. 1986 Chaotic streamlines in the ABC flows. *J. Fluid Mech.* **167**, 353–391.

Jimenez, J. 1980 On the visual growth of a turbulent mixing layer. *J. Fluid Mech.* **96**, 447–460.

Jones, S. W. & Aref, H. 1988 Chaotic advection in pulsed source–sink systems. *Phys. Fluids* **31**, 469–485.

Jones, S. W., Thomas, O. M. & Aref, H. 1989 Chaotic advection by laminar flow in a twisted pipe. *J. Fluid Mech.* **209**, 335–357.

Khakhar, D. V., Rising, O. & Ottino, J. M. 1986 Analysis of chaotic mixing in two model systems. *J. Fluid Mech.* **172**, 419–451.

Ottino, J. M. 1989 *The Kinematics of Mixing: Stretching, Chaos, and Transport.* Cambridge University Press.

Panton, R. L. 1979 *Incompressible Flow.* John Wiley & Sons.

Pierrehumbert, R. T. & Widnall, S. E. 1981 The structure of organized vortices in a free shear layer. *J. Fluid Mech.* **102**, 301–313.

Roberts, F. A. 1985 Effects of a periodic disturbance on structure and mixing in turbulent shear layers and wakes. Ph.D. thesis, Graduate Aeronautical Laboratories, California Institute of Technology.

Rom-Kedar, V., Leonard, A. & Wiggins, S. 1990 An analytical study of transport, mixing and chaos in an unsteady vortical flow. *J. Fluid Mech.* **214**, 347–394.

Solomon, T. H. & Gollub, J. P. 1988 Chaotic particle transport in time-dependent Rayleigh–Benard convection. *Phys. Rev.* A **38**, 6280–6286.

Stuart, J. T. 1967 On finite amplitude oscillations in laminar mixing layers. *J. Fluid Mech.* **29**, 417–440.

Tennyson, J. L., Cary & Escande, D. F. 1986 Change of the adiabatic invariant due to separatrix crossing. *Phys. Rev. Lett.* **56**, 2117–2120.

Timofeev, A. V. 1978 On the constancy of an adiabatic invariant when the nature of the motion changes. *Sov. Phys. JETP* **48**, 656–659.